JEM Journal of Experimental Medicine

ARTICLE

Loss of tRNA-modifying enzyme Elp3 activates a p53-dependent antitumor checkpoint in hematopoiesis

Adeline Rosu[1], Najla El Hachem[2], Francesca Rapino[2], Kevin Rouault-Pierre[3,4], Joseph Jorssen[1], Joan Somja[5], Eve Ramery[6], Marc Thiry[7], Laurent Nguyen[8], Maarten Jacquemyn[9], Dirk Daelemans[9], Christopher M. Adams[10], Dominique Bonnet[3], Alain Chariot[11,12], Pierre Close[2,12], Fabrice Bureau[1,12], and Christophe J. Desmet[1,12]

The hematopoietic system is highly sensitive to perturbations in the translational machinery, of which an emerging level of regulation lies in the epitranscriptomic modification of transfer RNAs (tRNAs). Here, we interrogate the role of tRNA anticodon modifications in hematopoiesis by using mouse models of conditional inactivation of Elp3, the catalytic subunit of Elongator that modifies wobble uridine in specific tRNAs. Loss of Elp3 causes bone marrow failure by inducing death in committing progenitors and compromises the grafting activity of hematopoietic stem cells. Mechanistically, Elp3 deficiency activates a p53-dependent checkpoint in what resembles a misguided amino acid deprivation response that is accompanied by Atf4 overactivation and increased protein synthesis. While deletion of p53 rescues hematopoiesis, loss of Elp3 prompts the development of p53-mutated leukemia/lymphoma, and inactivation of p53 and Elongator cooperatively promotes tumorigenesis. Specific tRNA-modifying enzymes thus condition differentiation and antitumor fate decisions in hematopoietic stem cells and progenitors.

Introduction

The differentiation of hematopoietic stem cells (HSCs) into lineage-restricted progenitors and, eventually, mature blood and immune cells is a very finely controlled process. In addition to being regulated at the gene expression level, hematopoiesis is particularly sensitive to perturbations in the translational machinery, which may lead to diseases from anemia to hematologic cancer (Guzzi et al., 2018; Khajuria et al., 2018; Liu et al., 2017; Signer et al., 2014). An emerging level of translational regulation lies in the regulation of the pool of transfer RNAs (tRNAs) by chemical modifications, constituting what may be considered a tRNA epitranscriptome. Indeed, with ∼100 modifications reported to date, tRNA molecules are hot spots of modifications, catalyzed by a large number of tRNA-modifying enzymes (El Yacoubi et al., 2012; Krutyhołowa et al., 2019). Modifications outside the tRNA anticodon impact the maturation, localization, stability, aminoacylation, or ribosome binding of target tRNAs (El Yacoubi et al., 2012; Krutyhołowa et al., 2019). On the other hand, modifications in the anticodon that occur on the wobble base in position 34 are mostly understood as playing a role in improving or modifying the decoding activity of target tRNAs (Johansson et al., 2008; Krutyhołowa et al., 2019). Recent evidence indicates that specific tRNA modifications play important roles in hematopoiesis. Indeed, pseudouridylation at the 5′ end of specific tRNAs by the enzyme PUS7 is involved in the repression of global protein synthesis in HSCs through pseudouridylated tRNA fragments (Guzzi et al., 2018). Loss of PUS7 activity deregulates protein synthesis in HSCs and compromises their differentiation and engraftment capability, a mechanism

[1]Laboratory of Molecular and Cellular Immunology, GIGA-Stem Cells, GIGA-Research, Liege University, Liège, Belgium; [2]Laboratory of Cancer Signaling, GIGA-Stem Cells, GIGA-Research, Liege University, Liège, Belgium; [3]Haematopoietic Stem Cell Laboratory, Francis Crick Institute, Queen Mary University of London, London, UK; [4]Centre for Haemato-Oncology, Barts Cancer Institute, Queen Mary University of London, London, UK; [5]Laboratory of Pathological Anatomy and Cytology, Centre Hospitalier Universitaire, GIGA-Stem Cells and GIGA-Neurosciences, Liege University, Liège, Belgium; [6]Department of Functional Sciences, Faculty of Veterinary Medicine, Liege University, Liège, Belgium; [7]Laboratory of Cellular and Tissular Biology, GIGA-Stem Cells and GIGA-Neurosciences, Liege University, Liège, Belgium; [8]Laboratory of MolecularRegulation of Neurogenesis, GIGA-Stem Cells and GIGA-Neurosciences, Liege University, Liège, Belgium; [9]KU Leuven Department of Microbiology, Immunology and Transplantation, Laboratory of Virology and Chemotherapy, Rega Institute, Leuven, Belgium; [10]Departments of Internal Medicine and Molecular Physiology and Biophysics, University of Iowa, Iowa City, IA; [11]Laboratory of Medical Chemistry, GIGA-Stem Cells, Liege University, Liège, Belgium; [12]Walloon Excellence in Life Sciences and Biotechnology, Wavres, Belgium.

Correspondence to Christophe J. Desmet: christophe.desmet@uliege.be.

that could also be involved in myelodysplastic syndromes (Guzzi et al., 2018).

The impact on hematopoiesis of other tRNA modifications, notably those in the anticodon, remains unknown. In this regard, an interesting group of tRNA-modifying enzymes is composed of the Elongator and cytosolic thiouridylase (Ctu)-1/2 complexes, which modify the wobble uridine (U_{34}) in specific cytosolic tRNAs. Elongator is composed of a dimeric assemblage of six subunits (Elongator protein [Elp]1–6), of which Elp1 is the scaffolding subunit and Elp3 the catalytic subunit. Elongator catalyzes a first enzymatic reaction, leading to the formation of 5-methoxycarbonylmethyl or 5-carbamoylmethyl side chains on U_{34} in 11 cytosolic tRNA species. The unrelated dimeric Ctu1/2 complex catalyzes a further 2-thiolation of U_{34} in four specific tRNAs (Arg^{UCU}, Lys^{UUU}, Gln^{UUG}, and Glu^{UUC}; El Yacoubi et al., 2012). Although full inactivation of Elongator leads to embryonic death in mice (Cheishvili et al., 2011), its inactivation in restricted mammalian cell lineages generates distinct nonlethal outcomes (Delaunay et al., 2016; Ladang et al., 2015; Laguesse et al., 2015).

From a molecular standpoint, mammalian phenotypes linked to the loss of U_{34}-modifying enzymes have so far been mainly attributed to perturbed protein synthesis, leading to two main outcomes: first, to proteotoxic stress triggering signaling through the unfolded protein response (UPR) branch of the integrated stress response (ISR; Laguesse et al., 2015) or, second, to loss-of-function phenotypes due to impaired expression of specific proteins whose mRNA is enriched in the codons Lys^{UUU}, Gln^{UUG}, and Glu^{UUC} (Delaunay et al., 2016; Ladang et al., 2015; Rapino et al., 2018). Yet, observations in yeast indicate that U_{34} modifications are also sensed as metabolic cues of sulfur amino acid availability (Laxman et al., 2013; Gupta et al., 2019; Gupta and Laxman, 2020). Their loss activates the yeast Gcn4 metabolic stress response pathway, a functional orthologue of the mammalian metabolic adaptor activating-transcription factor-4 (Atf4; Chou et al., 2017; Zinshteyn and Gilbert, 2013).

Here, to study the role of tRNA wobble base modifications in hematopoiesis, we investigated the consequences of hematopoietic-restricted genetic deletion of the Elp3 catalytic subunit of Elongator in mice.

Results

Loss of Elongator activity in hematopoietic progenitors causes hematopoietic failure in mice

We generated a mouse model of Elongator deficiency in the hematopoietic system by crossing $Elp3^{fl/fl}$ mice with $Vav1\text{-}iCre^{T/+}$ mice (Fig. S1 A). The resulting $Elp3^{fl/fl}$ $Vav1\text{-}iCre^{T/+}$ ($Elp3^{HscKO}$) mice displayed a loss of Elp3 protein expression, along with a detectable reduction in 2-thiolation and methoxycarbonylmethyl tRNA uridine modifications in total bone marrow (BM) cells (Fig. S1, B and C). Since there were no noticeable differences in baseline hematopoiesis of $Elp3^{fl/fl}$ and $Vav1\text{-}iCre^{T/+}$ mice (Fig. S1 D), $Elp3^{fl/fl}$ mice were further used as controls. $Elp3^{HscKO}$ mice were born at Mendelian ratios but had reduced lifespans (Fig. 1 A). $Elp3^{HscKO}$ mice usually displayed paler limb extremities (Fig. 1 B) resulting from severe anemia with RBC poikilocytosis (Fig. 1, C and D). In addition to having progressively aggravating anemia (Fig. 1 D), $Elp3^{HscKO}$ mice were panleukopenic (Fig. 1 D and Fig. S1, E and F). Only blood concentrations of platelets, which were initially reduced in $Elp3^{HscKO}$ mice, normalized in older individuals (Fig. 1 D).

BM in adult $Elp3^{HscKO}$ mice was hypoplastic (Fig. 1, E and F) and displayed features reminiscent of severe BM failure. For instance, cell surface expression of c-kit was downregulated in hematopoietic stem and progenitors (HSPC; lineage $[Lin]^-$ $Sca1^+$ $c\text{-}Kit^+$) and in Lin^- $Sca1^-$ $c\text{-}Kit^+$ cells (enriched in myeloid lineage-committed progenitors and referred to as MyPs from here onward; Fig. 1 G), while mast cells accumulated in the BM of $Elp3^{HscKO}$ mice (Fig. S1 G). Numbers of MyPs and lymphoid lineage-committed progenitors were starkly reduced at all ages tested in $Elp3^{HscKO}$ mice (Figs. 1 H and S1 H). In contrast, long-term HSCs (LT-HSCs), as well as short-term HSCs and $CD150^+$ multipotent progenitors (MPPs), tended to accumulate with age in $Elp3^{HscKO}$ mice (Figs. 1 I and S1 I). On the other hand, $CD150^-$ MPP populations were depressed in younger $Elp3^{HscKO}$ mice, although $CD150^-CD48^-$ MPPs recovered with age, paralleling the increase in $CD150^+$ lineage $(Lin)^-$ $Sca1^+$ $c\text{-}Kit^+$ progenitor (LSK) populations (Fig. 1 I). Altogether, the hematopoietic phenotype of $Elp3^{HscKO}$ mice indicated a pan-lineage blockade of differentiation of hematopoietic progenitors, resulting in BM failure.

Intrinsic requirement of Elongator activity for progenitor survival and HSC reconstitution activity

In $Elp3^{HscKO}$ mice, HSCs but not MyPs displayed increased cell cycling activity (Fig. 2, A and B), and HSCs and MPPs exited quiescence (Fig. 2 B and Fig. S2, A and B). On the other hand, staining with JC-1 as a measure of cell viability indicated consistently reduced mitochondrial membrane potential in Elp3-deficient MyPs and $CD150^-CD48^+$ MPPs, whereas other HSPC subsets were less impacted (Figs. 2 C and S2 C). MyPs and $CD150^-CD48^+$ MPPs being the subtypes consistently depleted in $Elp3^{HscKO}$ mice (Fig. 1, H and I), these results indicate that loss of Elongator blocked hematopoiesis by impairing the viability of MyPs and subsets of upstream HSPCs.

To challenge the functionality of Elp3-deficient HSCs, we tested the engraftment potential of $Elp3^{HscKO}$ LT-HSCs in competitive transplantation assays (Fig. 2 D). $Elp3^{HscKO}$ cells had a low contribution to mature blood cell production, but also to the HSPC and MyP pools in most grafted recipient mice (Fig. 2, E and F). Yet, short-term grafting experiments indicated that Elongator-deficient HSCs retained capacity to home to the BM (Fig. S2 D). To further test the impact of Elp3 on HSC biology, we generated an inducible model of Elongator inactivation ($Elp3^{fl/fl}$ $Mx1\text{-}Cre^{T/+}$ mice). The contribution of $Elp3^{fl/fl}$ $Mx1\text{-}Cre^{T/+}$ cells to mature blood cell production rapidly declined after Elp3 deletion (Fig. 2, G and H) and there was a marked depletion of $Elp3^{fl/fl}$ $Mx1\text{-}Cre^{T/+}$ MyPs and MPPs after 4 mo (Figs. 2 I and S2 E). In contrast, the pool of $Elp3^{fl/fl}$ $Mx1\text{-}Cre^{T/+}$ LT-HSCs and short-term HSCs was comparable to that of control $Elp3^{fl/fl}$ HSCs in grafted mice (Figs. 2 I and S2 E) and the majority of these cells remained quiescent (Figs. 2 J and S2 E). Hence, these data support the notion that exit from quiescence of HSCs in $Elp3^{HscKO}$ mice was mostly a compensatory attempt at restoring blood production. Importantly,

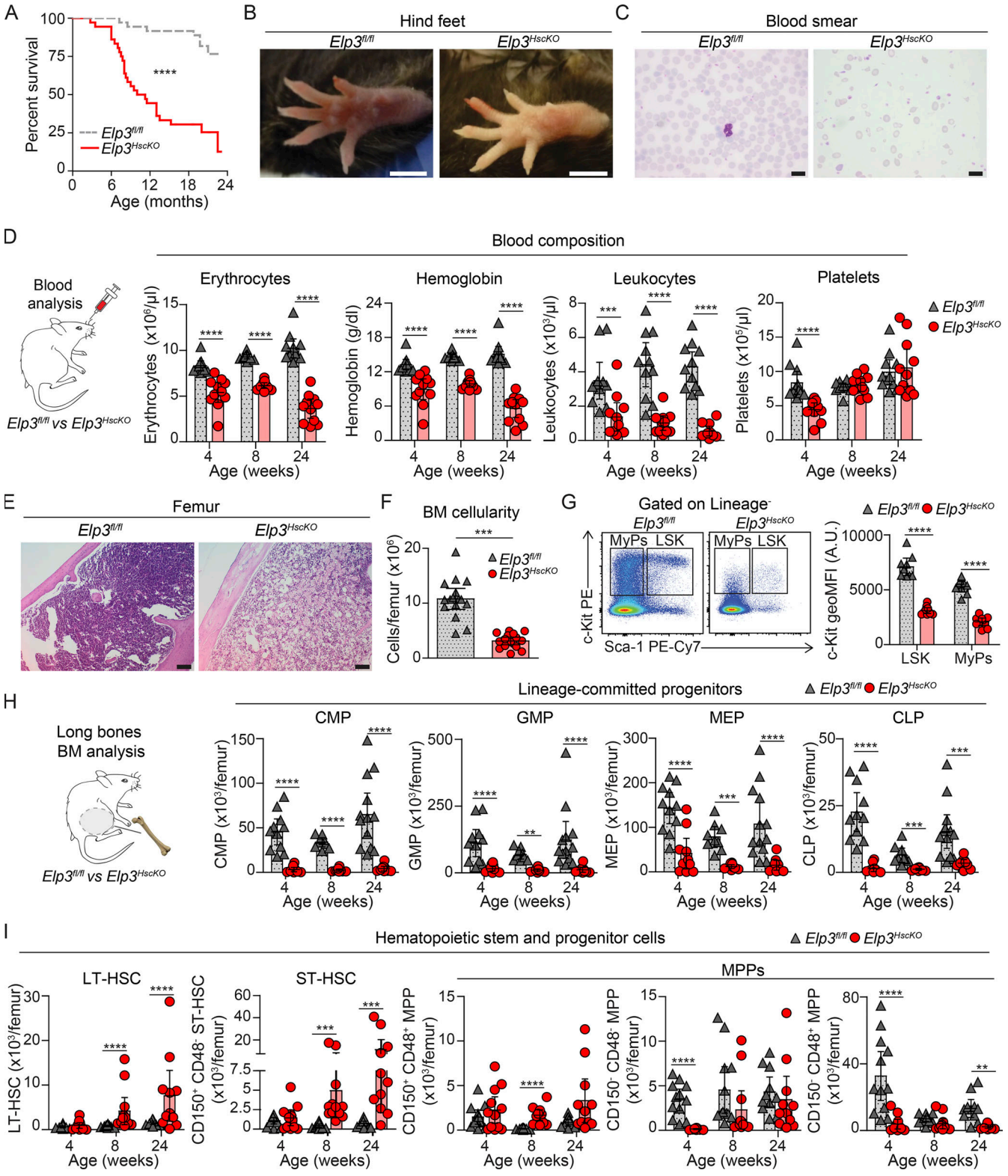

Figure 1. **Inactivation of Elongator in hematopoietic progenitors causes hematopoietic failure. (A)** Survival curve of *Elp3*$^{fl/fl}$ and *Elp3*^{HscKO} mice (Mantel-Cox test, *n* = 36/group, pool of two experiments). **(B)** Representative hind foot (scale bars, 0.2 cm). **(C)** Blood smear of 6-mo-old *Elp3*$^{fl/fl}$ and *Elp3*^{HscKO} mice (scale bars, 10 µm). **(D)** Hemocytometric comparison of blood composition in *Elp3*$^{fl/fl}$ and *Elp3*^{HscKO} mice (two-way ANOVA, *n* = 11/group, pool of three experiments). **(E)** Representative sections of femurs of 24-wk-old *Elp3*$^{fl/fl}$ and *Elp3*^{HscKO} mice (scale bars, 100 µm). **(F)** BM cell count in femurs of 8-wk-old *Elp3*$^{fl/fl}$ and *Elp3*^{HscKO} mice (Mann-Whitney test, *n* = 16/group, pool of four experiments). **(G)** Flow cytometric profile (left) and surface c-Kit expression level (right) of LSK cells and MyPs in the BM of 8-wk-old *Elp3*$^{fl/fl}$ and *Elp3*^{HscKO} mice (two-way ANOVA, *n* = 9–10/group, pool of three experiments). **(H and I)** Count of lineage-committed progenitors (H) and of LSK multipotent progenitors (I) in the femurs of *Elp3*$^{fl/fl}$ and *Elp3*^{HscKO} mice (two-way ANOVA, *n* = 9–12/group, pool of three experiments). CLP, common lymphoid progenitor; CMP, common myeloid progenitor; GMP, granulocyte-monocyte progenitor; MEP, megakaryocyte-erythrocyte progenitor; ST-HSC, short-term HSC; LT-HSC, long-term HSC. **, P < 0.01; ***, P < 0.001; ****, P < 1.10^{-4}.

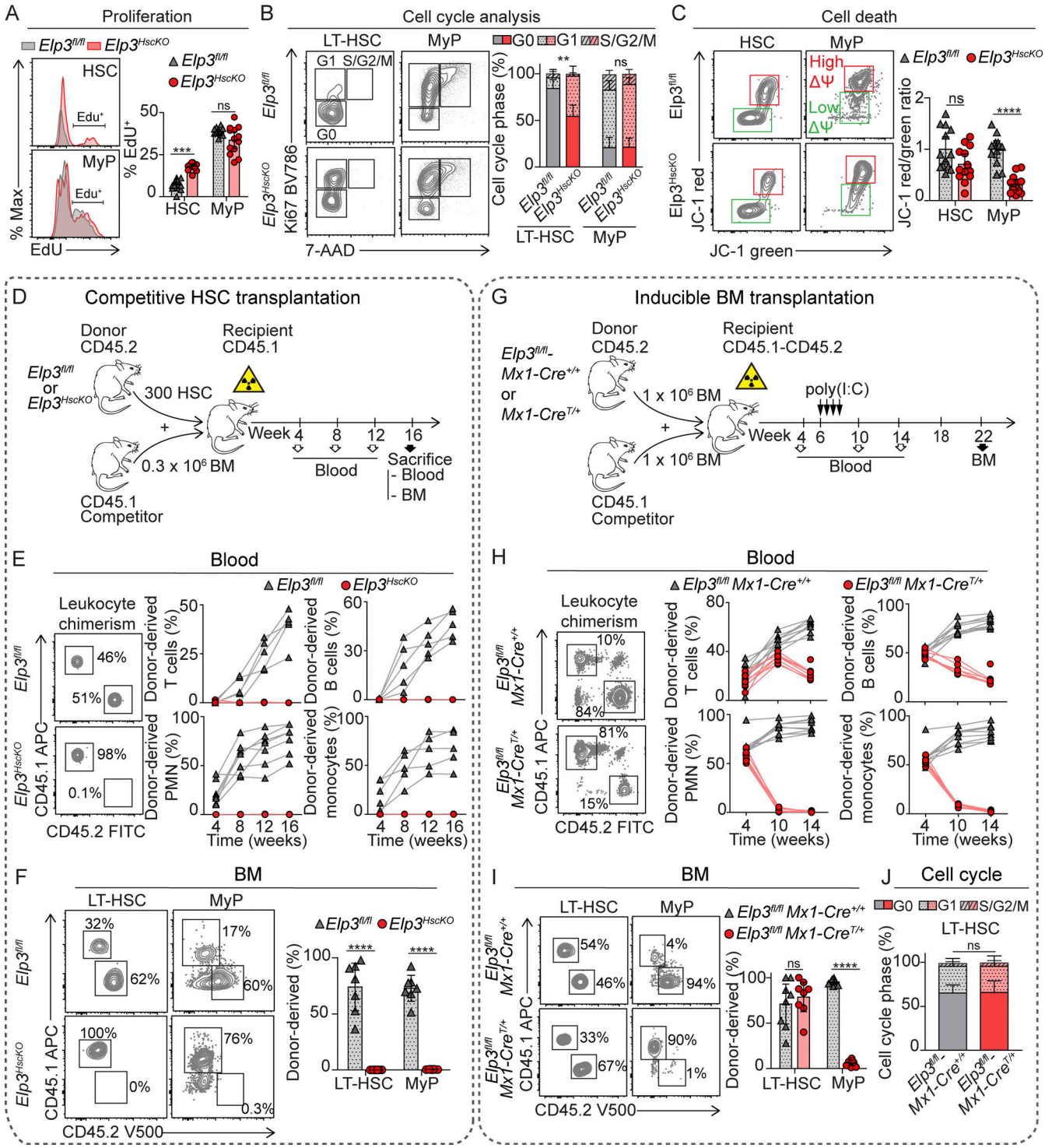

Figure 2. **Loss of Elp3 activity kills committed progenitors and impairs HSC grafting potential. (A)** Flow cytometric profile (left) and percentages of proliferating cells (right) based on EdU incorporation (two-sided pairwise *t* tests with Bonferonni correction, *n* = 13–14/group, pool of three experiments). **(B)** Flow cytometric cell cycle profile (left) and percentages of cells in each stage (right; two-sided pairwise *t* tests comparison of percent G0 with Bonferonni correction, *n* = 9/group, pool of three experiments). **(C)** Flow cytometric profile (left) and ratio of red-on-green signal intensities (normalized to the mean ratio in control cells in each experiment; Δψ, mitochondrial membrane potential; *n* = 13/group, pool of three experiments, two-way ANOVA) in LT-HSCs and MyPs of *Elp3*$^{fl/fl}$ and *Elp3*^{HscKO} mice. **(D)** Experimental outline of competitive transplantation assays of *Elp3*$^{fl/fl}$ or *Elp3*^{HscKO} LT-HSCs. **(E and F)** Flow cytometric profile (left) and resulting *Elp3*$^{fl/fl}$ or *Elp3*^{HscKO} blood leukocyte (E) or BM LT-HSC and MyP (F) chimerism through time (right) in transplanted recipient mice (data representative of two experiments, two-way ANOVA). **(G)** Experimental outline of competitive transplantation assays of *Elp3*$^{fl/fl}$ or *Elp3*$^{fl/fl}$ *Mx1-Cre*$^{T/+}$ BM, followed by poly(I:C)-induced allele recombination. **(H and I)** Flow cytometric profile (left) and resulting *Elp3*$^{fl/fl}$ or *Elp3*$^{fl/fl}$ *Mx1-Cre*$^{T/+}$ blood leukocyte (H) and BM LT-HSC and MyP (I) chimerism through time (right) in transplanted recipient mice (data representative of three experiments, two-way ANOVA). **(J)** Cell cycle analysis as in B (two-sided pairwise *t* tests comparison of percent G0 with Bonferonni correction, *n* = 8–9/group, representative of two experiments). ns, not significant; ***, P < 0.001; ****, P < 1.10^{-4}. PMN, polymorphonuclear.

following grafting to secondary recipient mice, *Elp3*$^{fl/fl}$ *Mx1-Cre*$^{T/+}$ total BM cells, which had already lost Elp3 expression, displayed a marked long-term engraftment deficit similar to that of LT-HSCs from *Elp3*^{HscKO} mice (Fig. S2, F–H). Taken together, these data show that Elongator is intrinsically required for the long-term reconstitution capacity of HSCs.

Loss of Elongator activity upregulates global protein synthesis in hematopoietic progenitors

To study the consequences of Elongator deficiency on the proteome of hematopoietic progenitors, we performed integrated comparative proteomic analyses on control and *Elp3*^{HscKO} MyPs (Fig. 3 A and Table S1). Only 54 proteins were significantly downregulated in *Elp3*^{HscKO} MyPs. This limited set was not enriched for any particular gene ontology biological process (in PANTHERdb and Webgestalt). It also contained only a few proteins with a clear prominent mRNA use of codons Lys^{AAA}, Gln^{CAA}, and Glu^{GAA} (Fig. 3 B), and we identified none of these proteins as obvious candidates that could be involved in the phenotype of Elp3-deficient hematopoiesis. In contrast, upregulated proteins in Elp3-deficient MyPs formed a highly interconnected network (protein–protein interaction enrichment $P < 1.10^{-16}$; Fig. 3 C) enriched in proteins playing a role in translation (Fig. 3, C–E).

The above data suggested that Elp3-deficient hematopoietic progenitors counterintuitively harbored enhanced protein synthesis. Indeed, two independent approaches, namely O-propargyl puromycin incorporation assays in vivo and L-homopropargyl-glycine incorporation assays in vitro, confirmed that global protein synthesis rates were increased in *Elp3*^{HscKO} progenitors (Fig. 4 A). To assess changes in the translatome of *Elp3*^{HscKO} progenitors, we performed polysome profiling on MyPs (Fig. 4 B). We detected only 51 enriched and 78 depleted transcripts in heavy polysomes of *Elp3*^{HscKO} relative to control MyPs, even though we used a low threshold of a 30% difference (Fig. 4 C). Validating our polysome profiling analysis, enriched transcripts in polysomes of *Elp3*^{HscKO} MyPs comprised significantly more transcripts, with higher representation of A-ending codons decoded by Elongator-modified tRNAs than the coding genome average ($P = 1.10^{-6}$; Fig. 4 D). Indeed, in Elp3-deficient cells, elongation slowdown leads to increased ribosome density on mRNAs rich in codons translated by Elongator-modified tRNAs, such as Dek (Fig. 4, C and D; Delaunay et al., 2016; Rapino et al., 2018). Nonetheless, out of 12 transcripts enriched in Lys^{AAA}, Gln^{CAA}, and Glu^{GAA} codons that were detected and quantified in comparative proteomics (Fig. 3), all, including Dek, had protein expression levels close or, for a majority, slightly superior to those predicted by changes in their mRNA (Fig. 4 D), indicating that their protein expression was not compromised by the mild translational perturbation they underwent in MyPs. Hence, Elp3-deficient progenitors displayed increased protein synthesis with limited perturbations in their translatome.

Upregulation of protein synthesis and our polysome profiling analysis argued against the notion that *Elp3*^{HscKO} progenitors develop ER stress and activate the UPR or the ISR. In addition, we did not detect changes in Ser^{51}-eIF2α phosphorylation, the convergence point of ISR signaling and a key signaling event in the UPR, in Elp3-deficient HSCs and MyPs (Fig. 5, A and B; and Fig. S3 A). There also was no noticeable upregulation in MyPs of the mRNA coding for Gadd34 (also known as Ppp1r15a) or of classical ER-associated degradation genes, which respond to the Atf6- and Xbp1-mediated arms of the UPR (Fig. 5 C), nor were there visible changes in Xbp1 splicing (Fig. 5 D) or in the ultrastructure of the ER (Fig. 5 E) in MyPs of *Elp3*^{HscKO} mice. The PERK/ATF4/CHOP pathway has been proposed as the major mediator of hematopoietic progenitor death in response to UPR/ISR activation (Rouault-Pierre et al., 2013; van Galen et al., 2014); however, mice harboring a codeletion of Chop (encoded by *Ddit3*) and *Elp3* (*Ddit3*$^{-/-}$ *Elp3*$^{fl/fl}$ *Vav1-iCre*$^{T/+}$ mice) had a hematological phenotype similar to that of *Elp3*^{HscKO} mice (Fig. 5, F–I). Altogether, Elp3-deficient progenitors failed to display signs of major translational hindrance and instead harbored increased protein synthesis.

Deficiency in Elongator coactivates p53 and Atf4 in hematopoietic progenitors in a response resembling amino acid deprivation

To more broadly dissect the response of hematopoietic progenitors to deficient Elongator activity, we resorted to RNA sequencing on HSCs and MyPs as representatives of undifferentiated and differentiating progenitors, respectively. Elp3-deficient HSCs mostly upregulated gene expression signatures associated with cell cycling, in line with their increased proliferation. Elp3-deficient MyPs, on the other hand, displayed upregulation of gene sets associated with inflammatory processes (Fig. S3, B and C). PC2 of a principal component analysis separated control HSC and MyP transcriptomes from their *Elp3*^{HscKO} counterparts (Fig. 6 A), prompting us to examine their common transcriptional response (Table S2). Both HSCs and MyPs upregulated gene expression programs associated with cell death (Fig. 6 B) and induction of some of its key target genes (*Bbc3*, *Cdkn1a*, *Perp*, *Pmaip1*, etc.) suggested that the cell death and cell cycle regulator p53 was activated in Elp3-deficient hematopoietic progenitors (Fig. 6, C and D). Confirming this hypothesis, Elp3-deficient BM progenitors displayed increased protein expression of p53 in the absence of changes in Ser^{15} phosphorylation (Fig. 5, E and F; and Fig. S3, D–F). Of note, proapoptotic genes, like *Perp*, *Pmaip1* (encoding Noxa), and *Bbc3* (encoding Puma), were more strongly induced in MyPs than in HSCs, whereas *Cdkn1a* (encoding p21), which is often cytoprotective, was more strongly induced in HSCs (Fig. 6 D).

In addition, both HSCs and MyPs upregulated gene expression programs associated with mTORC1 activity (Fig. 6 B). We noticed that most of the mTORC1 target genes actually corresponded to direct target genes of Atf4, another major stress-responsive transcription factor (Han et al., 2013; Wortel et al., 2017). Indeed, ranked gene set enrichment analysis (GSEAR) indicated a strong enrichment in Atf4 target genes in the transcriptional response of HSCs and MyPs (Fig. 6, C and G). Of note, genes composing the Atf4 gene signature were generally more strongly induced in Elp3-deficient MyPs than in HSCs (Fig. 6 G). Confirming this hypothesis, all tested subsets of Elp3-deficient BM progenitors displayed increased levels of Atf4 protein (Fig. 6 H and Fig. S3, G and H). Noticeably, hematopoietic

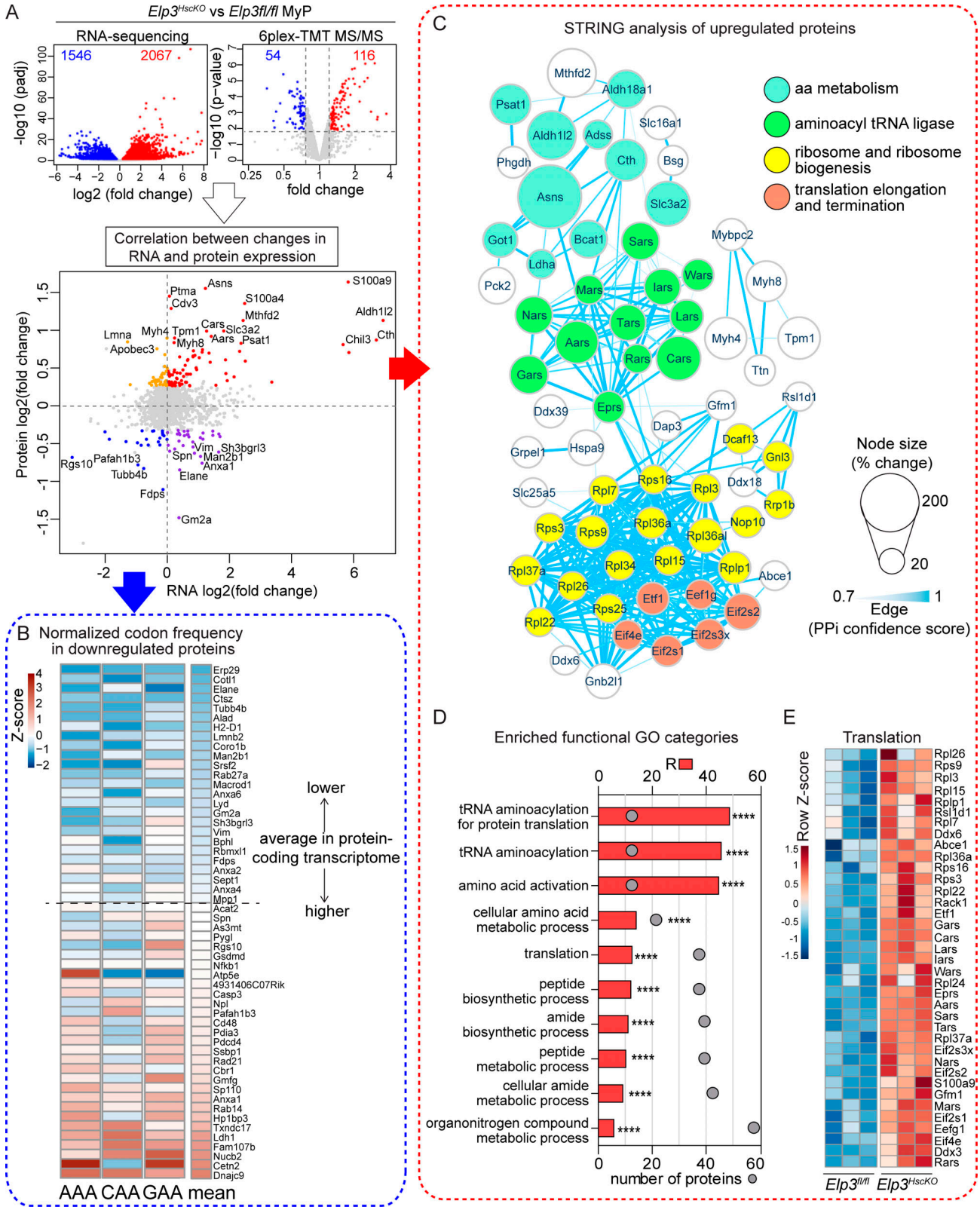

Figure 3. **Inactivation of Elongator induces a coordinated protranslational response in committed progenitors. (A)** Volcano plots of the changes in mRNA levels (left) and in protein levels (right) in *Elp3*$^{fl/fl}$ and *Elp3*^{HscKO} MyPs, and correlation between changes in protein and mRNA levels (bottom). **(B)** Heatmap of normalized frequencies of codons Lys^{AAA}, Gln^{CAA}, and Glu^{GAA} in the cds of proteins downregulated in Elp3-deficient MyPs. **(C)** Interaction network of the proteins upregulated in Elp3-deficient MyPs. **(D)** GO enrichment analysis in Webgestalt on the set of genes coding for the proteins upregulated in Elp3-deficient MyPs (R, fold enrichment; ****, P < 1.10^{-4}). **(E)** Heatmap of the expression of proteins belonging to GO category "Translation" in D in *Elp3*$^{fl/fl}$ or *Elp3*^{HscKO} MyPs.

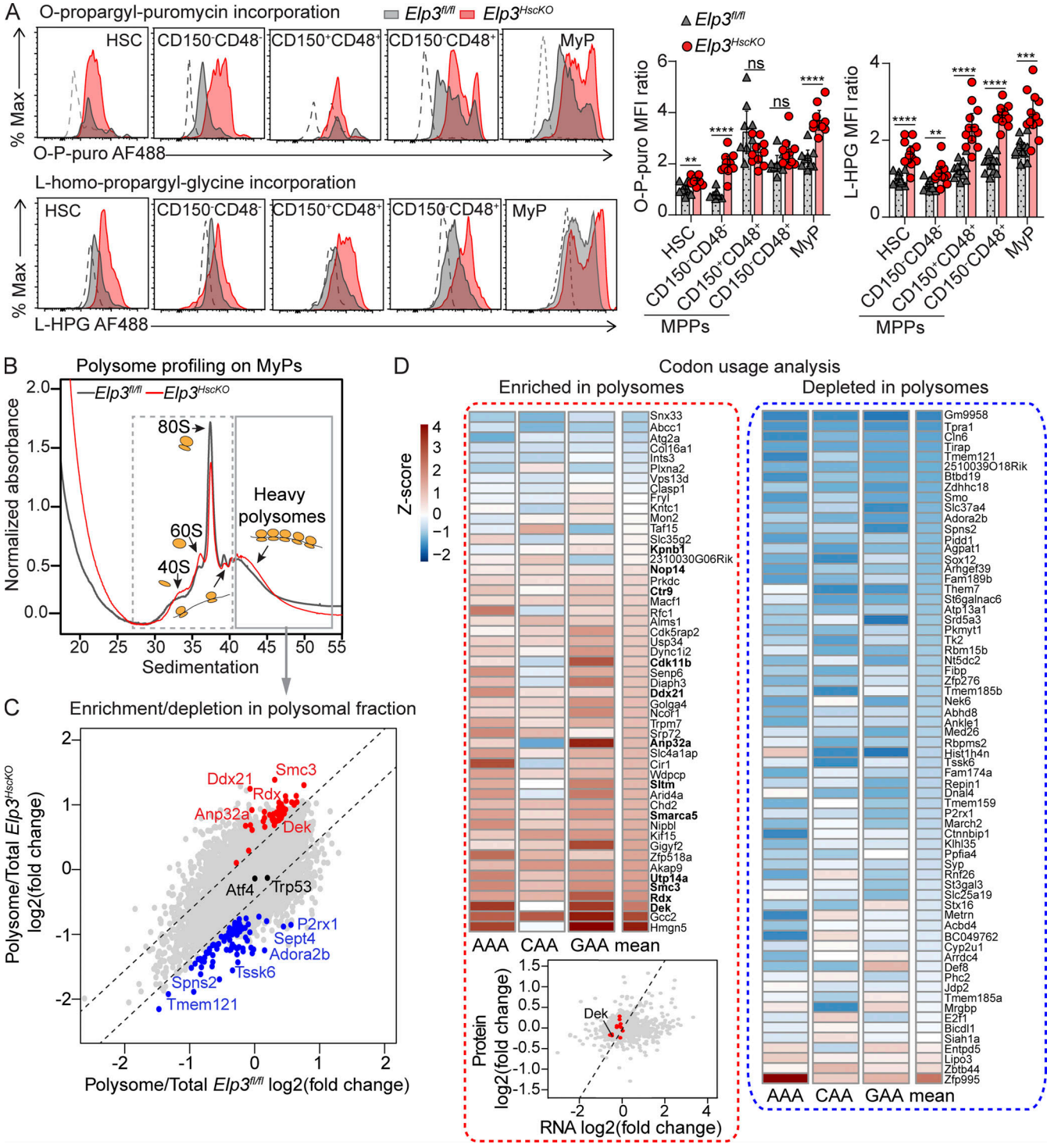

Figure 4. **Loss of Elp3 upregulates global protein synthesis in hematopoietic progenitors. (A)** Flow cytometric profile of in vivo O-propargyl puromycin (O-p-Puro) incorporation (upper left) or in vitro L-homopropargylglycine (L-HPG) incorporation (lower left) and normalized signal intensity (right) in *Elp3*$^{fl/fl}$ and *Elp3*^{HscKO} HSCs and MyPs (two-way ANOVA, *n* = 10 and 12/group, data pooled from two and three experiments, respectively). **(B)** Experimental outline and representative polysome profile in *Elp3*$^{fl/fl}$ and *Elp3*^{HscKO} MyPs. **(C)** Correlation of transcript enrichment in polysomal fractions in *Elp3*$^{fl/fl}$ and *Elp3*^{HscKO} MyPs (*n* = 3 independent experiments). Transcripts that deviated by at least 30% between *Elp3*^{HscKO} and *Elp3*$^{fl/fl}$ MyPs were considered as significantly enriched (red) or depleted (blue). **(D)** Frequencies in codons Lys^{AAA}, Gln^{CAA}, and Glu^{GAA} in selected transcripts in C and correlation between protein and mRNA changes (same data as in Fig. 3 A). ns, not significant; **, P < 0.01; ***, P < 0.001; ****, P < 1.10^{-4}.

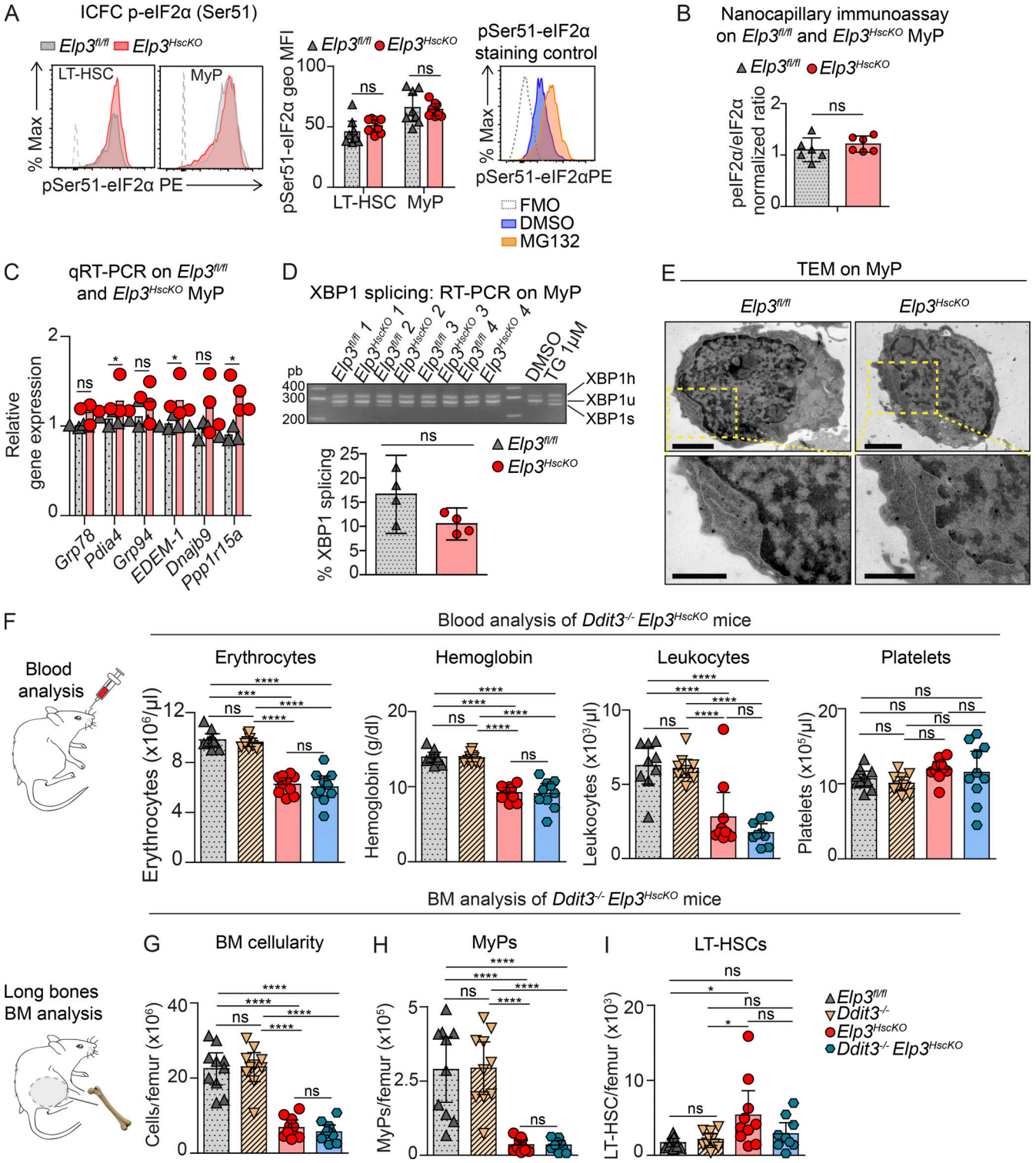

Figure 5. **Elp3-deficicent progenitors do not show signs of activation of the UPR or ISR. (A)** Flow cytometric profile of cytoplasmic phosphoSer[51]-eIF2α (left) and normalized signal intensity (center) in *Elp3*$^{fl/fl}$ and *Elp3*^{HscKO} HSCs and MyPs (two-way ANOVA, n = 8/group, data pooled from three experiments; right: positive control, total BM treated for 4 h with 20 µM MG132). **(B)** Ratio of phospho-Ser[51]eIF2α on total eIF2α assessed by nanocapillary immunoassay in Wes analysis on protein extracts of *Elp3*$^{fl/fl}$ and *Elp3*^{HscKO} MyPs. Vinculin was used as loading control for quantification (two-sided t test, pool of two experiments). **(C)** Real-time RT-PCR of UPR genes in MyPs from *Elp3*$^{fl/fl}$ and *Elp3*^{HscKO} mice (*Tbp*, *Ubc*, and *B2m* as reference, Wilcoxon test, n = 3–4/group). **(D)** Ratio of Xbp1 spliced (XBP1s) on Xbp1 unspliced (XBP1u) RT-PCR band intensity in *Elp3*$^{fl/fl}$ and *Elp3*^{HscKO} MyPs. XBP1h, hybrid amplified from XBP1s and XBP1u. **(E)** Representative transmission electron microscopy of *Elp3*$^{fl/fl}$ and *Elp3*^{HscKO} MyPs and zoom on ER (upper panel scale bars, 2 µm; lower panels, 1 µm). **(F–I)** Hemocytometric analysis (F), BM cellularity (G), and flow cytometric analysis of the numbers of MyPs (H) and LT-HSCs (I) in *Elp3*$^{fl/fl}$, *Ddit3*$^{-/-}$, *Elp3*^{HscKO}, and *Ddit3*$^{-/-}$ *Elp3*^{HscKO} mice (two-way ANOVA, n = 10/group, data pooled from three experiments). FMO, fluorescence minus one; TEM, transmission electron microscopy. ns, not significant; *, P < 0.05; ***, P < 0.001; ****, P < 1.10^{-4}.

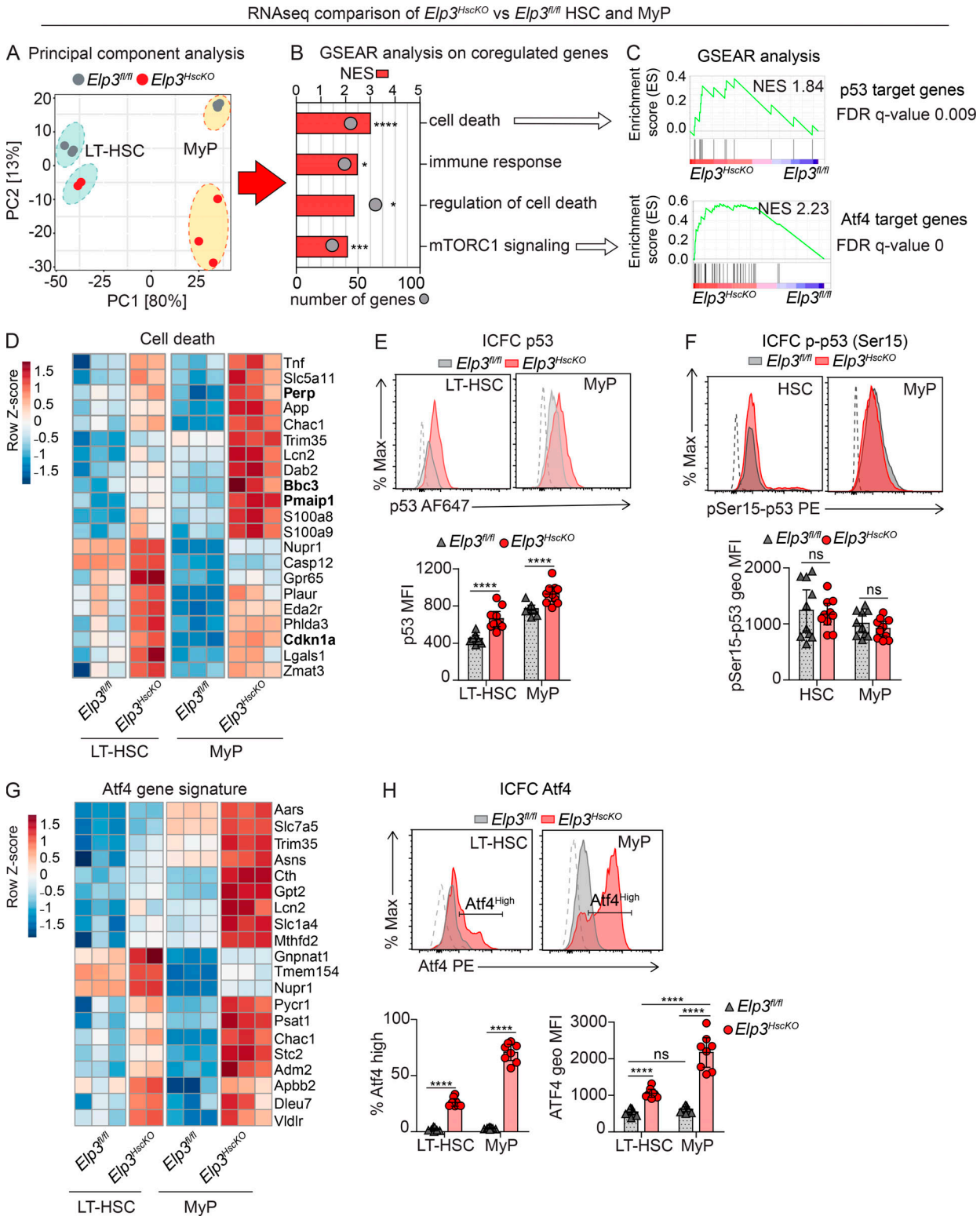

Figure 6. **Elp3 deletion activates p53 and Atf4 stress responses in hematopoietic progenitors. (A)** Principal component analysis on the transcriptome of *Elp3*$^{fl/fl}$ and *Elp3*^{HscKO} LT-HSCs and MyPs. **(B and C)** GSEAR analysis of upregulated Hallmark gene sets (B) and p53 and Atf4 target genes (C) in the transcriptome of both *Elp3*^{HscKO} LT-HSCs and MyPs compared with their *Elp3*$^{fl/fl}$ counterparts (*, familywise error rate [FWER] $P < 0.05$; ***, $P < 1.10^{-3}$; ****, $P < 1.10^{-4}$). **(D)** Heatmap of the expression of the top 20 leading edge genes in the "Cell death" GO gene set in *Elp3*$^{fl/fl}$ and *Elp3*^{HscKO} LT-HSCs and MyPs. **(E and F)** Intracellular flow cytometric (ICFC) profile of p53 (E) and phospho-Ser^{15} p53 (F) and signal intensity in *Elp3*$^{fl/fl}$ and *Elp3*^{HscKO} HSCs and MyPs (two way-ANOVA, $n = 10$/group, data pooled from three experiments). **(G)** Heatmap of the expression of the top 20 leading edge Atf4 target genes in *Elp3*$^{fl/fl}$ and *Elp3*^{HscKO} LT-HSCs and MyPs. **(H)** Intracellular flow cytometric profile of Atf4 expression and comparison of the percentages of Atf4^{high} cells (left) and Atf4 signal intensity (right) in *Elp3*$^{fl/fl}$ and *Elp3*^{HscKO} HSCs and MyPs (ns, not significant; ****, $P < 1.10^{-4}$ in a two-way ANOVA, $n = 8–9$/group, data pooled from two experiments). FDR, false discovery rate. ns, not significant; ****, $P < 1.10^{-4}$.

progenitor subsets that underwent cell death in *Elp3*^{HscKO} mice also displayed the highest levels of Atf4 in *Elp3*^{HscKO} mice.

Among well-established overlapping functions, Atf4 and p53 are mostly known to help cells cope with oxidative stress and nutrient deprivation (Kruiswijk et al., 2015; Tang et al., 2015; Wortel et al., 2017). Elp3-deficient progenitors had reduced levels of total and normal levels of mitochondrial reactive oxygen species (Fig. 7 A), ruling out oxidative stress as an activator of p53 and Atf4. Yeast deficient in U_{34}-modifying enzymes mount a response resembling sulfur amino acid deprivation through the Atf4-like Gcn4 pathway (Gupta and Laxman, 2020). Suggesting a similar aberrant response in Elp3-deficient BM, the transcriptomic response of *Elp3*^{HscKO} MyPs and HSCs was enriched in signatures of amino acid deprivation comprising Atf4 and p53 target genes (Fig. 7, B and C).

While the mechanism of activation of p53 in response to amino acid deprivation remains elusive, Atf4 has mostly been documented to be upregulated in this context through activation of the GCN2 arm of the ISR as well as through poorly understood transcriptional mechanisms (Dey et al., 2010; Tang et al., 2015). As shown above, we did not detect signs of ISR activation in Elp3-deficient progenitors. We also did not find evidence that Atf4 upregulation may be due to mTORC1 (Ben-Sahra et al., 2016; Park et al., 2017) or MYC signaling (Tameire et al., 2019). Indeed, activation of Atf4 through the mTORC1 pathway depends on increased phosphorylation of 4EBP1. Yet, phosphorylation of 4EBP1 increased only marginally in *Elp3*^{HscKO} HSCs and not in MyPs, while expression of total 4EBP1 increased in all progenitors, leading to a relative decrease in the ratio of phospho-4EBP1 on total 4EBP1 (Fig. 7 D). We also observed that protein expression of c-Myc was increased in *Elp3*^{HscKO} HSCs, which cycle more but not consistently in MyPs (Fig. 7 E). Rather, we found that Atf4 was upregulated at the mRNA level (Fig. 7 F) while the transcript of Atf4—and that of Trp53—did not show any significant increase in ribosomal density in Elp3-deficient MyPs (Fig. 4 C). This suggests that transcriptional mechanisms are primarily responsible for Atf4 protein upregulation in *Elp3*^{HscKO} progenitors. Altogether, we hypothesized that p53 and Atf4 are coactivated as part of a maladaptive amino acid deprivation-like response in Elp3-deficient progenitors.

p53 is an antitumor checkpoint in Elongator-deficient hematopoietic progenitors

p53 being the most obvious candidate involved in BM failure in *Elp3*^{HscKO} mice, we generated mice with a hematopoietic deficiency for both *Elp3* and *Trp53*. Homozygous deletion of *Trp53* normalized blood composition, BM cellularity, and numbers of MyPs and HSPCs in *Elp3*$^{fl/fl}$ *Trp53*$^{fl/fl}$ *Vav1-iCre*$^{T/+}$ (*Elp3/Trp53*^{HscDKO}) mice (Fig. 8, A–D). The hematologic phenotype of *Elp3*^{HscKO} mice was thus caused by a p53-dependent checkpoint.

To further assess the effect of the loss of p53 on the functionality of Elp3-deficient HSPCs, we compared BM recovery in *Elp3*^{HscKO} and *Elp3/Trp53*^{HscDKO} mice after initial myeloablation through treatment with 5-fluorouracil (5-FU; Fig. 8, E–G). 9 d after 5-FU treatment, BM cellularity and MyP numbers were severely depressed in 5-FU–treated *Elp3*^{HscKO} mice compared with controls (Fig. 8 G), indicative of impaired HSPC repopulating capacity. In contrast, *Elp3/Trp53*^{HscDKO} mice recovered similarly to *Elp3*$^{fl/fl}$ and *Trp53*^{HscKO} mice (Fig. 8, F and G). Hence, the loss of p53 was sufficient to rescue the repopulating activity of Elp3-deficient HSPCs.

To ascertain that p53 activation was indeed related to the loss of tRNA U_{34} modifications, and not to putative tRNA-independent functions of Elp3, we tested the consequences of silencing CTU2, one of the two subunits of the cytosolic thiouridylase complex that further modifies U_{34} in selected tRNA targets of Elongator (El Yacoubi et al., 2012) in the TF-1 human HSPC cell line (Fig. 8 H). Like Elp3-deficient mouse BM progenitors, TF-1 cells responded to silencing of ELP3 or CTU2 by upregulating their global protein synthesis rate (Fig. 8 I) and increasing protein expression of p53 (Fig. 8 J), mimicking the response of Elp3-deficient mouse BM progenitors.

To better understand the effect of p53 deletion on Elp3-deficient progenitors, we analyzed the transcriptome of MyPs from *Elp3/Trp53*^{HscDKO} mice. Principal component analysis indicated a nearly complete normalization of the transcriptome of Elp3-deficient MyPs following the loss of p53 activity (Fig. S4 A). Nevertheless, the 277 genes that remained coregulated in *Elp3*^{HscKO} and *Elp3/Trp53*^{HscDKO} MyPs were again highly enriched in Atf4 target genes (Fig. S4, B–D; and Table S3). In line with these observations, the Atf4 protein still accumulated in *Elp3/p53*^{HscDKO} BM progenitors, although less than in *Elp3*^{HscKO} mice, and still in the absence of changes in phosphor-Ser^{51}-eIF2α (Fig. S4, E and F). Expression of Atf4 target genes was also lower in *Elp3/p53*^{HscDKO} MyPs compared with their *Elp3*^{HscKO} counterparts (Fig. S4 D). Partial persistence of the Atf4 response in the absence of p53 hence indicates that the loss of Elongator also triggered the Atf4 stress response independently of p53. Our analyses indicate that p53 activation amplified the Atf4 response induced by loss of Elongator.

Because Atf4 itself is required for normal hematopoiesis (Masuoka and Townes, 2002), we could not delete Atf4 to test its involvement directly in the phenotype of *Elp3*^{HscKO} mice. We nonetheless tested whether Atf4 overactivation plays a protective or a detrimental role in BM progenitors undergoing p53 activation. We generated mice overexpressing Atf4 in the entire hematopoietic system (*Rosa26*$^{fl\text{-}STOP\text{-}fl\text{-}Atf4/+}$ *Vav1-iCre*$^{T/+}$ *Atf4*^{HscTG} mice), which displayed Atf4 protein levels in HSCs and MyPs that were comparable to those attained in *Elp3*^{HscKO} mice (Fig. 8 K). BM function after 5-FU exposure was severely compromised in *Atf4*^{HscTG} mice but was rescued by hemizygous deletion of *Trp53* (Fig. 8, L–N). The response of *Atf4*^{HscTG} mice to 5-FU phenocopied that of *Elp3*^{HscKO} mice (Fig. 8, L–N), supporting the notion that Atf4 overactivation and p53 cooperate in eliciting the demise of stressed BM progenitors.

Even though deleting p53 remarkably normalized the functionality of BM progenitors in *Elp3/Trp53*^{HscDKO} mice, these mice reached ethical end points within a maximum of 6 mo (Fig. 9 A) because of the development of tumors involving the thymus, spleen, and/or the liver (Fig. S5, A and B). This was significantly faster than their control *Trp53*^{HscKO} counterparts and prompted us to assess tumor incidence in *Elp3*^{HscKO} mice. We observed that ∼50% of *Elp3*^{HscKO} mice reaching ethical end points had developed tumors involving the thymus, spleen, and/or liver (Figs. 9 B

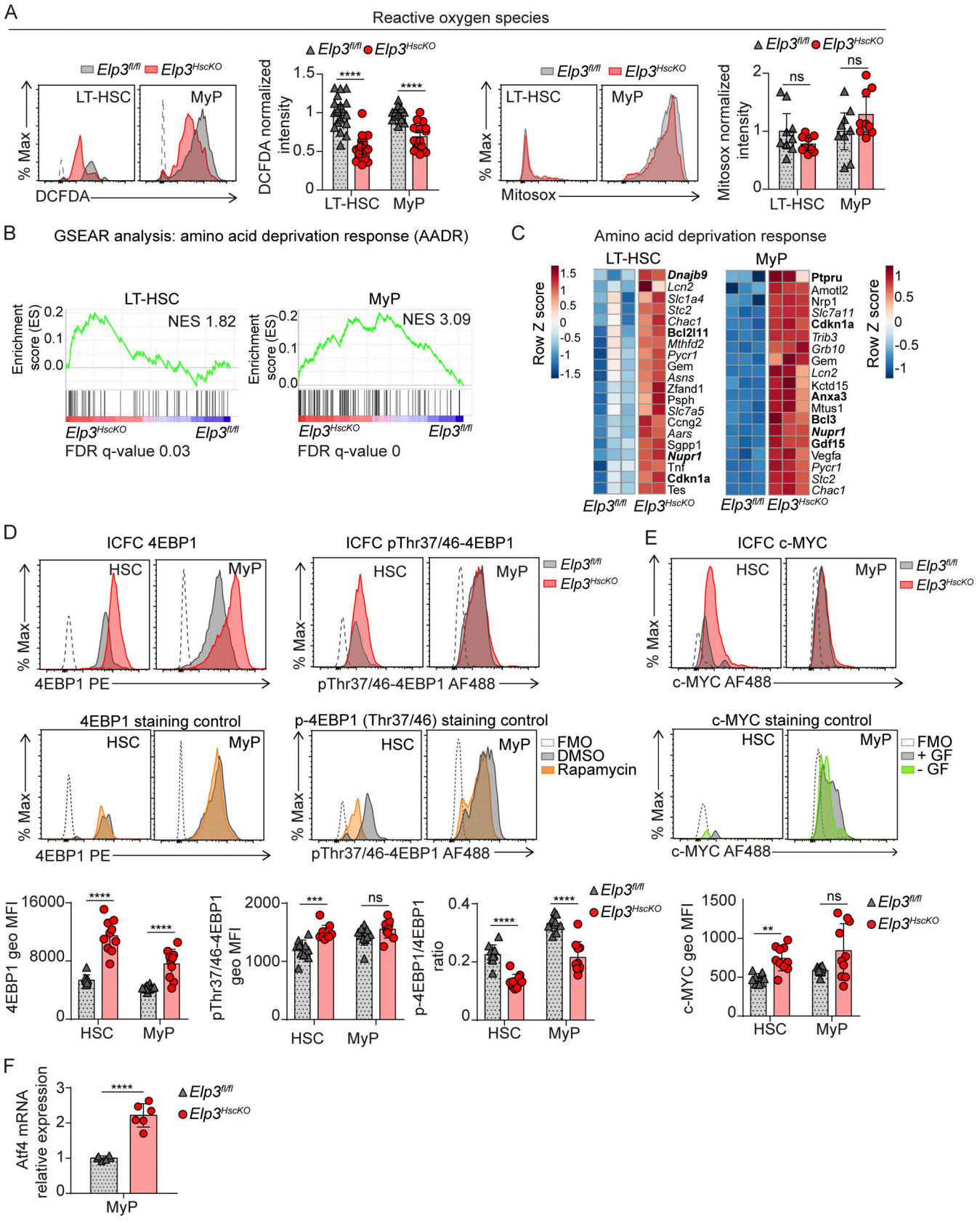

Figure 7. **Deficiency in Elongator activates an amino acid deprivation-like response coordinated by p53 and Atf4 in hematopoietic progenitors. (A)** Flow cytometric profiles and normalized signal intensity of dichlorodihydrofluorescein diacetate (DCFDA; left) and Mitosox (right) staining in *Elp3*$^{fl/fl}$ and *Elp3*^{HscKO} LT-HSCs and MyPs (two-way ANOVA, *n* = 9–18/group, data pooled from three experiments). **(B and C)** GSEAR analysis of the enrichment in amino

acid deprivation response genes (B; Tang et al., 2015) and heatmaps of the expression of the respective top 20 leading edge genes in the amino acid deprivation response gene set (C) in the transcriptome of *Elp3*^{HscKO} LT-HSCs (left) and MyPs (right). **(D and E)** Intracellular flow cytometric (ICFC) profiles and signal intensity of total 4EBP1, phospho-Thr$^{37/46}$ 4EBP1 (D) and c-Myc (E) in *Elp3*$^{fl/fl}$ and *Elp3*^{HscKO} HSCs and MyPs (two-way ANOVA, n = 10/group, data pooled from three experiments; staining controls: WT BM progenitors treated for 4 h with 100 nM rapamycin or cultured overnight in the absence of growth factors [GF]). **(F)** *Atf4* mRNA expression in *Elp3*$^{fl/fl}$ and *Elp3*^{HscKO} MyPs (two way-ANOVA, n = 6/group; data from Figs. 4 C and S3 B). FMO, fluorescence minus one; NES, normalized enrichment score. ns, not significant; **, P < 0.01; ***, P < 0.001; ****, P < 1.10^{-4}.

and S5 C). Histologic examination of tumors in *Elp3*^{HscKO} and *Elp3/Trp53*^{HscDKO} mice showed an accumulation of lymphoblasts in the spleen, bone marrow, liver, and thymus (Fig. 9 C), suggesting increased incidence of T-cell acute lymphoblastic leukemia/lymphoma.

Since Elongator inactivation blocked HSPC differentiation through p53-dependent mechanisms, we tested whether tumor development in *Elp3*^{HscKO} mice was associated with p53 mutation. Indeed, targeted exon sequencing of the *Trp53* gene identified *Trp53* mutations in >90% of tumors from *Elp3*^{HscKO} mice (Fig. 9 D). Remarkably, all mutations occurred in conserved regions in the DNA-binding domain of Trp53 (Fig. 9 D). Homology of the mutated positions with a systematic positional mutation screen of human TP53 predicts that >80% of tumors arising in *Elp3*^{HscKO} mice harbored p53 loss-of-function mutations (Kotler et al., 2018). Hence, inactivation of Elongator by itself promoted hematologic malignancy in mice, the development of which was associated with and accelerated by the loss of p53.

Discussion

The epitranscriptome, via the information conveyed by base modifications in RNA molecules, plays increasingly recognized roles in stem cell fate decisions and differentiation. The hematopoietic system, through its elevated sensitivity to perturbations in the translational apparatus, is unsurprisingly emerging as one of the major adult target organs of epitranscriptomic regulation (Chua et al., 2020). Here, we report that the loss of enzymes that modify wobble uridine in selected tRNAs deeply affects fate decisions in HSCs and their differentiating progeny.

In some aspects, Elongator-deficient hematopoiesis is reminiscent of the defects experienced by HSCs deficient for PUS7 (Guzzi et al., 2018). Indeed, PUS7-deficient HSCs experience deregulated protein synthesis, blocked differentiation, and impaired grafting activity (Guzzi et al., 2018). PUS7-deficient HSCs display a phenotype very similar to that of other models of increased protein synthesis in HSCs (Signer et al., 2014, 2016); therefore, we deem it likely that the loss of function of Elongator-deficient HSCs too is at least in part attributable to their deregulated protein synthesis. Yet, progenitor lethality has not been observed in response to increased protein synthesis in BM progenitors (Guzzi et al., 2018; Signer et al., 2014, 2016), and p53-mediated cell death in our model is hence likely independent of the impact of Elongator deficiency on global translation. Together, studies on PUS7 and Elongator concur to support the notion that the tRNA epitranscriptome is an essential level of regulation of normal hematopoiesis, in part but not solely, through the control of protein synthesis rates in HSCs.

Our analyses did not detect major translational defects that could be responsible for the phenotype of Elp3-deficient hematopoiesis. Notably, we did not detect signs of UPR activation and protein synthesis rates increased in HSCs and committing progenitors, suggesting an absence of proteotoxic stress. Previous reports identified a higher sensitivity of HSCs compared with committing progenitors to ER stress–induced cell death or to even modest increases in protein mistranslation (Hidalgo San Jose et al., 2020; van Galen et al., 2014). Yet, we observed an inverse phenotype in Elp3-deficient hematopoiesis, with a lethal impact on committing progenitors, but a more limited impact on quiescent HSCs. The demise of committing progenitors following the loss of Elongator was associated with the activation of a p53-dependent proapoptotic gene signature, while a more cytoprotective p21 response developed in HSCs (Fig. 9 E). The choice between a proapoptotic or prosurvival outcome of p53 activation depends on a wide variety of parameters (Kruiswijk et al., 2015). In Elongator-deficient hematopoiesis, the progenitor subsets that were depleted were those displaying the highest basal level of protein synthesis in control mice and the strongest Atf4 activation in *Elp3*^{HscKO} mice. Furthermore, activation of p53 itself contributed to Atf4 overactivation, and we could show that overactivation of Atf4 favors p53-dependent killing of stressed hematopoietic progenitors. Together, these observations suggest that progenitor death in *Elp3*^{HscKO} mice results from the cooperation between p53 and overactivation of Atf4, the latter being conditioned by the cell's overall protein synthetic or metabolic activity. The fact that Atf4 may directly activate gene expression of the p53 proapoptotic target genes *Bbc3* and *Pmaip1*, which are upregulated in Elp3-deficient MyPs, brings further support to this hypothesis (Qing et al., 2012).

How Elp3 deletion coactivates p53 and Atf4 remains to be further explored, but our data may be reminiscent of the response resembling amino acid deprivation that develops in yeast deficient for U_{34}-modifying enzymes (Laxman et al., 2013; Gupta et al., 2019; Gupta and Laxman, 2020). Indeed, p53 and Atf4 together control hallmark responses to individual amino acid deprivation in mammalian cells (Tang et al., 2015). While the mechanisms activating p53 in response to amino acid deprivation are currently unknown, Atf4 is induced in this context through the GCN2 branch of the ISR that reacts to unloaded tRNAs, but also through upregulation of the Atf4 mRNA (Tang et al., 2015). We thus foresee that the loss of Elongator triggers Atf4 and p53 activation through as-yet-unknown signaling events in a misguided response to perceived amino acid deprivation. In yeast, U_{34} modifications—probably because they require sulfur-containing amino acids (cysteine and methionine) and s-adenosylmethionine as intermediates—have been coopted into sensors of methionine availability (Laxman et al.,

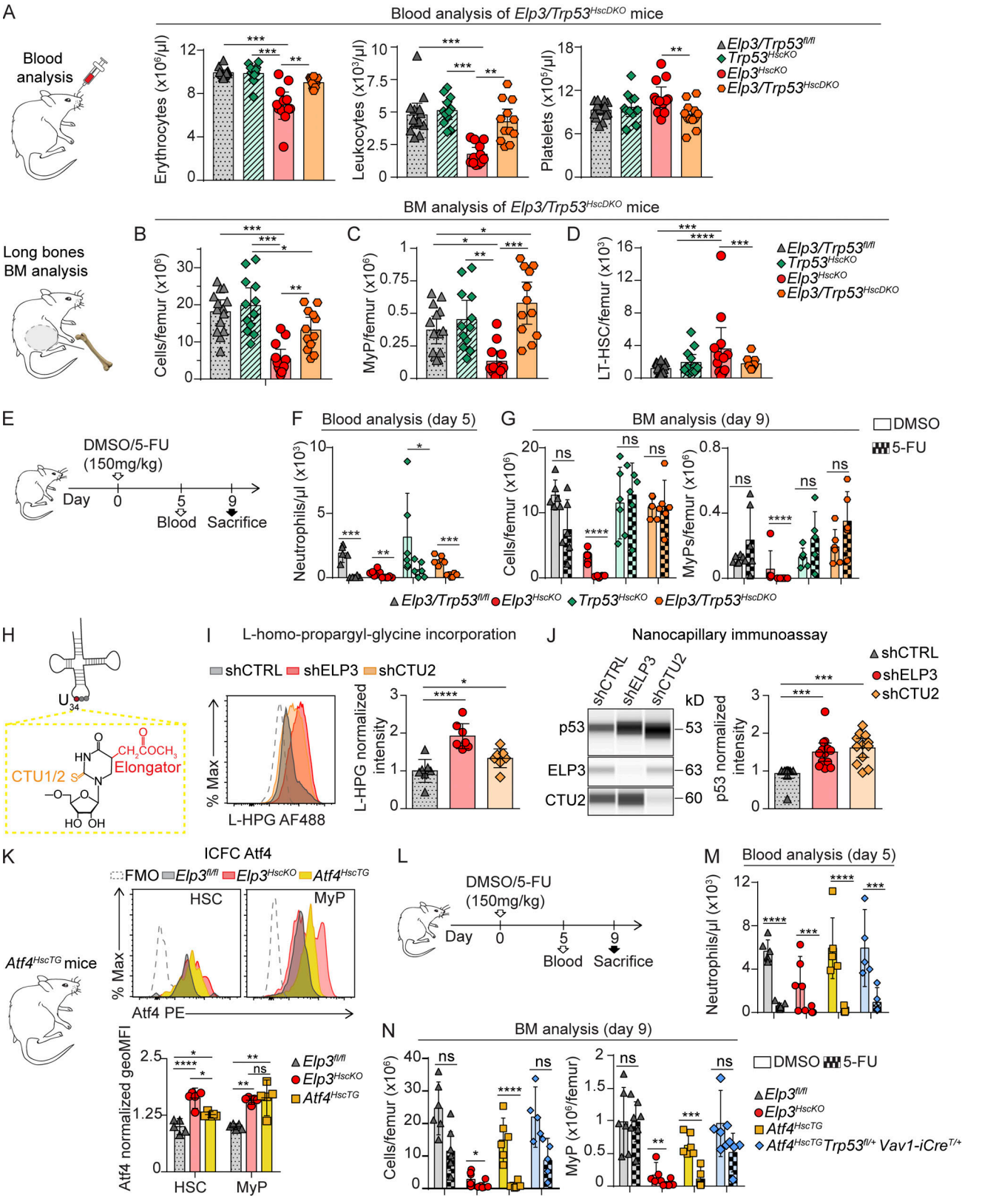

Figure 8. **Deletion of p53 rescues Elongator-deficient hematopoiesis. (A)** Hemocytometric comparison of RBCs, leukocytes, and platelets in *Elp3*$^{fl/fl}$, *Trp53*^{HscKO}, *Elp3*^{HscKO}, and *Elp3/Trp53*^{HscDKO} mice (ANOVA, *n* = 12–14/group, data pooled from three experiments). **(B–D)** Total BM (B), MyP (C), and LT-HSC (D) cell counts in the femur of *Elp3*$^{fl/fl}$, *Trp53*^{HscKO}, *Elp3*^{HscKO}, and *Elp3/Trp53*^{HscDKO} mice (ANOVA, *n* = 12–14/group, data pooled from three experiments). **(E–G)** Experimental outline (E), blood polymorphonuclear (PMN) concentrations (F), and total BM and MyPs counts (G) in 5-FU and excipient-treated *Elp3*$^{fl/fl}$, *Trp53*^{HscKO}, *Elp3*^{HscKO}, and *Elp3/Trp53*^{HscDKO} mice (two-sided pairwise *t* tests with Bonferroni correction, *n* = 6/group, pool of two experiments). **(H)** Depiction of

Elongator and CTU1/2 catalyzed tRNA modifications. **(I)** Flow cytometric profile of L-homopropargylglycine (L-HPG) incorporation (left) and normalized signal intensity (right) in shCTRL, shELP3, and shCTU2 TF-1 cells (two-way ANOVA, *n* = 7/group, data pooled from four experiments). **(J)** p53, ELP3, and CTU2 protein expression assessed by nanocapillary immunoassay with normalization module (left, representative pseudoblots; right, quantification of p53 protein expression) in shCTRL, shELP3, and shCTU2 TF-1 cells (two-way ANOVA, *n* = 13/group, data pooled from six experiments). **(K)** Intracellular flow cytometric profile (upper) and normalized intensities of nuclear Atf4 expression (lower) in *Elp3*$^{fl/fl}$, *Elp3*^{HscKO}, and Atf4^{HscTG} HSCs and MyPs (two-way ANOVA, *n* = 5/group, data pooled from two experiments). **(L–N)** Experimental outline (L), blood PMN concentrations (M), and total BM and MyPs counts (N) in 5-FU and excipient-treated *Elp3*$^{fl/fl}$, *Elp3*^{HscKO} and Atf4^{HscTG}, and *Atf4*^{HscTG} *Trp53*$^{fl/+}$ *Vav1-iCre*$^{T/+}$ mice (pairwise *t* tests with Bonferroni correction, *n* = 5–7/group, pool of two experiments). ns, not significant; *, P < 0.05; **, P < 0.001; ***, P < 0.001; ****, P < 1.10^{-4}.

2013). Our observations suggest that a similar co-optation of U_{34} modifications into sensors of sulfur amino acid availability could exist in mammalian cells and control cellular adaptation through p53 and Atf4 signaling. The nature of the putative sensor mechanism of (hypo)modified U_{34} remains to be identified in yeast and mammalian cells.

Loss of Elongator triggered p53-dependent BM failure, suggesting that p53 imposes stringent control on the presence of U_{34} modifications in HSPCs. Our observation that tumorigenesis of Elp3-deficient progenitors was accelerated in the absence of *Trp53* supports the notion that the failure of this quality control poses a risk of favoring malignant transformation in hematopoietic progenitors. Studies suggest that Elongator is required for tumor development or adaptation in breast and intestinal cancer as well as in melanoma (Delaunay et al., 2016; Ladang et al., 2015; Rapino et al., 2018). In contrast, inactivating mutations in Elp1 are key predisposing factors in specific types of medulloblastoma (Waszak et al., 2020), and a rare variant with predicted loss of function in the CTU2 gene has been associated with age-related clonal hematopoiesis in humans (Terao et al., 2020), suggesting a complex, cell type–dependent impact of U_{34} modifications on tumorigenesis. Interestingly, the *ELP5* gene, which encodes a subunit of Elongator, whose inactivation phenocopies *ELP1* or *ELP3* deletion (Close et al., 2012; Karlsborn et al., 2014), is located 0.5 Mbases away from the *TP53* gene on the 17p13 chromosomal region. Deletion of the syntenic *Elp5*-encompassing chromosomal region in mice accelerates the development of lymphoma compared with the deletion of p53 only (Liu et al., 2016), which is reminiscent of our present observations. The mechanisms through which loss of Elongator impact on tumorigenesis in the presence or absence of p53 are hence worth further investigating. Obvious protumoral candidates include increased protein synthesis and Atf4 overactivation, which have been shown to favor leukemia/lymphoma development (Signer et al., 2014; Tameire et al., 2019). Further work is therefore warranted into the protumoral effects of Elongator inactivation in the contexts of p53 mutation or 17p13 deletion.

Materials and methods

Mice

All experimental procedures and protocols were reviewed and approved by the Institutional Animal Care and Use Ethics Committee of Liege University. *Elp3*$^{fl/fl}$ mice have been described previously (Ladang et al., 2015). *Atf4*$^{fl/fl}$ mice were obtained from Prof. C.M. Adams (Department of Internal Medicine, University of Iowa, Iowa City, IA) and have been described previously (Ebert et al., 2012). *Vav1-iCre* mice (B6.Cg-*Commd10*$^{Tg(Vav1-icre)A2Kio}$/J), *Mx1-Cre* mice [B6.Cg-Tg(Mx1-cre)1Cgn/J], *Trp53*$^{fl/fl}$ mice (B6.129P2-*Trp53*^{tm1Brn}/J), *Rosa26*$^{fl\text{-}STOP\text{-}fl\text{-}Atf4}$ mice [B6.129X1-Gt(ROSA)26Sor$^{tm2(ATF4)Myz}$/J], *Ddit3*$^{-/-}$ mice [B6.129S(Cg)-Ddit3$^{tm2.1Dron}$/J], WT CD45.2 mice (C57BL/6J), and CD45.1 mice (B6.SJL-*Ptprc*^{a} *Pepc*^{b}/BoyJ) were obtained from The Jackson Laboratory. CD45.1-CD45.2 WT C57BL/6 mice were obtained by crossing CD45.1 with CD45.2 mice. *Elp3*^{HscKO} mice were obtained by crossing *Elp3*$^{fl/fl}$ mice with *Vav1-iCre* mice. *Trp53*^{HscKO} mice were obtained by crossing *Trp53*$^{fl/fl}$ mice with *Vav1-iCre* mice. Conditional inactivation of *Trp53* in *Elp3*^{HscKO} mice was achieved by crossing *Elp3*^{HscKO} mice with *Trp53*$^{fl/fl}$ mice. *Atf4*^{HscTG} mice were obtained by crossing *Rosa26*$^{fl\text{-}STOP\text{-}fl\text{-}Atf4}$ mice with *Vav1-iCre* mice, and inactivation of *Trp53* in *Atf4*^{HscTG} mice was achieved by crossing *Atf4*^{HscTG} mice with *Trp53*$^{fl/fl}$ mice. Conditional inactivation of *Ddit3* in *Elp3*^{HscKO} mice was achieved by crossing *Elp3*^{HscKO} mice with *Ddit3*$^{-/-}$ mice.

Balanced groups of male and female littermates were randomly assigned to experimental groups and were used at 8–12 wk of age, unless otherwise indicated. All mice were bred and housed in the specific pathogen–free facility of Liege University, except in experiments regarding the role of p53, for which *Trp53*$^{fl/fl}$ mice, their derived strains, and control *Elp3*$^{fl/fl}$ and *Elp3*^{HscKO} mice were housed on ventilated racks in the conventional mouse facility of Liege University. Ethical end points were considered to be reached when weight loss reached 20% of initial weight, or in case of apathy, hirsutism, or persistent labored breath.

Cell lines

TF-1 (cat#ACC-334) and B16 (cat#CRL-6322) cell lines were acquired from American Type Culture Collection. TF-1 cells were cultured at 37°C in RPMI 1640 medium (Gibco) with 20% FBS and 1% PenStrep (Gibco), supplemented with 10 ng/ml human recombinant GM-CSF (PeproTech).

Antibodies

Anti-mouse lineage cocktail APC (CD3, CD45R, Gr1, CD11b, and TER-119; clones 145-2C11, RA3-6B2, RB6-8C5, M1/70, and TER-119, cat#558074, Research Resource Identifier [RRID]:AB_1645213), anti-mouse CD117 PE and BV786 (clone 2B8, cat#561075, RRID: AB_10563204 and cat#564012, RRID:AB_2732005), anti-mouse Ly6A/E PE-Cy7 (clone D7, cat#561021, RRID:AB_2034021), anti-mouse CD34 FITC (clone RAM34, cat#553733, RRID:AB_395017), anti-mouse CD150 BV421 (clone Q8-480, cat#562811, RRID: AB_2732006), anti-mouse CD48 APC-Cy7 (clone HM48-1, cat#561242, RRID:AB_10644381), anti-mouse CD127 V450 and APC (clone SB/199, cat#561205, RRID:AB_10611870 and cat#564175, RRID:AB_2732843), anti-mouse CD16/CD32 APC-Cy7 (clone 2.4G2,

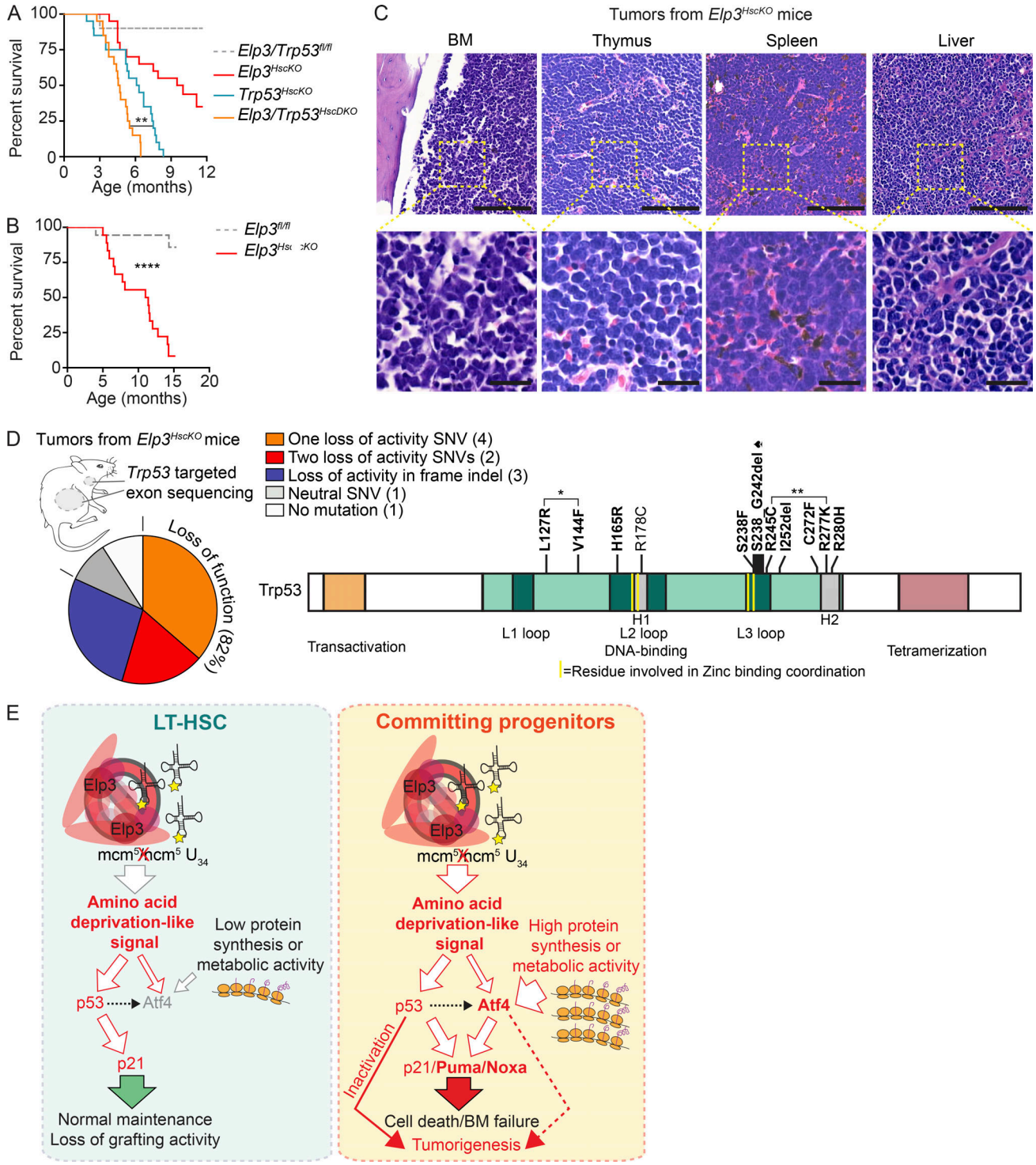

Figure 9. **p53 is activated as an antitumor checkpoint in Elongator-deficient hematopoietic progenitors**. **(A)** Survival curve of *Elp3*$^{fl/fl}$, *Trp53*^{HscKO}, *Elp3*^{HscKO}, and *Elp3/Trp53*^{HscDKO} mice (n = 20/group, Mantel-Cox test). **(B)** Survival curve of *Elp3*$^{fl/fl}$ and *Elp3*^{HscKO} mice (n = 18/group, Mantel-Cox test; cohort independent of that in Fig. 1 A). **(C)** Representative sections of tumors of *Elp3*^{HscKO} mice (upper panel scale bars, 100 µm; lower panels, 20 µm). **(D)** Types and prevalence of *Trp53* exon mutations in tumors of *Elp3*^{HscKO} mice (left panel, n = 11 thymus or spleen tumors from individual mice) and position and predicted consequences of said mutations on the p53 protein (right panel: * and **, mutations cooccurring in two individual tumors; spade symbol, deletion found in tumors of two individuals; bold, predicted loss-of-function mutations). **(E)** Model of the consequences of Elongator inactivation on HSCs and downstream progenitors. Loss of U34 modifications activates p53 and Atf4 in what resembles a misguided amino acid deprivation response. Possibly owing to their higher metabolic activity, MyPs overactivate Atf4 and a proapoptotic gene expression program, whereas HSCs are less impacted. Mutation of the p53 checkpoint favors tumorigenesis. SNV, single nucleotide variant; H, helix. **, $P < 0.01$; ****, $P < 1.10^{-4}$.

cat#560541, RRID:AB_1645229), anti-Ki67 BV786 (clone B56, cat#563756, RRID:AB_2732007), anti-mouse CD45 APC (clone 30-F11, cat#559864, RRID:AB_398672), anti-mouse CD45.2 FITC and V500 (clone 104, cat#561874, RRID:AB_10894189 and cat#562129, RRID:AB_10897142), anti-mouse CD19 PE (clone 1D3, cat#553786, RRID:AB_395050), anti-mouse CD11b BV421 (clone M1/70, cat#562605, RRID:AB_11152949), and anti-mouse Ly6G PE-Cy7 (clone 1A8, cat#560601, RRID:AB_1727562) were purchased from BD Biosciences. Anti-mouse lineage cocktail PE (CD3, CD45R, Gr1, CD11b, and TER-119; clones 145-2C11, RA3-6B2, RB6-8C5, M1/70, and TER-119, cat#133303, RRID:AB_1595553) was purchased from BioLegend. Anti-mouse CD150 PerCP-eFluor710 (clone mShad150, cat#46-1502-82, RRID:AB_2016699), anti-mouse CD45.1 APC (clone A20, cat#17-0453-81, RRID:AB_469397), anti-mouse CD3 APCe-Fluor780 (clone 17A2, cat#47-0032-82, RRID:AB_1272181), and F(ab′) 2 anti-rabbit IgG (H+L) secondary antibody PE (cat#12-4739-8, RRID: AB_1210761) were purchased from Thermo Fisher Scientific.

ELP3 rabbit mAb (clone D5H12, cat#5728, RRID:AB_11178379), β-actin mouse mAb (clone 8H10D10, cat#3700, RRID: AB_2242334), anti-mouse IgG, HRP-linked antibody (cat#7076, RRID:AB_330924), anti-rabbit IgG, HRP-linked antibody (cat#7074, RRID:AB_2099233), ATF4 rabbit mAb (clone D4B8, cat#11815S, RRID:AB_2616025), phospho-eIF2α (Ser51) rabbit mAb (clone D9G8, cat#3398S, RRID:AB_2096481), eIF2α rabbit mAb (clone D7D3, cat#5324S, RRID:AB_10692650), p53 Alexa Fluor 647 mouse mAb (clone 1C12, cat#2533, RRID:AB_2256294), phospho-p53 (Ser15) PE mouse mAB (clone 16G8, cat#8514, RRID:AB_11178384), 4E-BP1 PE rabbit mAb (clone 53H11, cat#34470, RRID:AB_2799054), phospho-4E-BP1 (Thr37/46) Alexa Fluor 488 rabbit mAb (clone 236B4, cat#2846, RRID: AB_2292749), and c-Myc Alexa Fluor 488 rabbit mAb (clone D84C12, Cat#12855, RRID:AB_2798045) were purchased from Cell Signaling Technology. TP53 anti-human mAb (clone DO-1, cat#sc-126, RRID: AB_628082) was purchased from Santa Cruz Biotechnology. CTU2 rabbit pAb (cat#NBP1-88457, RRID: AB_11054636) was purchased from Novus.

Histologic and cytologic BM and tumors analysis

Dissected femurs, thymus, spleen, and liver were fixed in 4% paraformaldehyde and paraffin embedded. Femurs were decalcified before paraffin embedding. Microsections of each specimen were fixed on glass slides, deparaffinized, and stained with hematoxylin and eosin. Sections were examined with an FSX100 microscope (Olympus). Smears of BM cells were prepared on glass slides and stained using the May Grünwald–Giemsa staining method.

Peripheral blood analysis

Blood was collected at sacrifice by retroorbital bleeding using sodium heparinized microhematocrit capillary tubes (Hirschmann). For serial blood analysis, blood was collected from the tail vein. Automated peripheral blood counts were obtained using a Cell-Dyn 3700. Peripheral blood was smeared on a slide and stained using the May Grünwald–Giemsa staining method.

Cell suspensions and flow cytometry

BM cells were isolated by flushing femurs, tibias, ilia, and humerus with PBS. Cells were filtered through a 70-μM cell strainer to obtain single-cell suspensions, and cell number was assessed by counting with a hemocytometer. For cell phenotyping, cells were stained for 30 min at 4°C. In experiments aimed at isolating LT-HSCs and MyPs, cells were first enriched for lineage-negative cells by magnetism-activated cell sorting using a lineage cell depletion kit (Miltenyi Biotec) before staining for cell-surface antigens. For Atf4, p53, phospho-p53 (Ser15), and c-Myc expression analysis, cells were first stained for cell-surface antigens, fixed, and permeabilized with FoxP3/Transcription Factor staining buffer set (Thermo Fisher Scientific) for 30 min at 4°C, and then labeled with p53 (1C12) Alexa Fluor 647, phospho-p53 (Ser15) (16G8) -PE, c-Myc (D84C12) Alexa Fluor 488 mouse mAbs, or ATF4 (D4B8) rabbit mAb (Cell Signaling Technology) at room temperature for 45 min. ATF4 staining was followed by incubation with PE anti-rabbit IgG secondary antibody (Thermo Fisher Scientific). For intracytoplasmic phospho-eIF2α (Ser51), 4E-BP1, and phospho-4E-BP1 expression analysis, cells were first stained for cell-surface antigens, fixed, and permeabilized with Intracellular Fixation & Permeabilization Buffer Set (Thermo Fisher Scientific) and labeled with 4E-BP1 (53H11) -PE, phospho-4E-BP1 (Thr37/46) (236B4), Alexa Fluor 488, or phospho-eIF2α (Ser51) rabbit mAb (clone D9G8; Cell Signaling Technology). Phospho-eIF2α (Ser51) staining was followed by incubation with PE anti-rabbit IgG secondary antibody (Thermo Fisher Scientific).

For quantification of reactive oxygen species, after staining for cell-surface antigens, cells were incubated at 37°C for 20 min in 500 μl preheated PBS plus 3% FBS supplemented with dichlorodihydrofluorescein diacetate (Thermo Fisher Scientific; final concentration 5 μM) or Mitosox Red Superoxide Indicator (Thermo Fisher Scientific; final concentration 10 μM), and then washed twice in preheated PBS plus 3% FBS.

For blood lymphocyte analysis, blood was incubated 15 min at room temperature in RBC lysis buffer (0.1 mM EDTA, 150 mM NH_4Cl, 10 mM $KHCO_3$) before staining.

Cell phenotyping was performed on a FACSCANTO II or a FACSFortessa and cell sorting on a FACSARIA III (BD Biosciences). Forward scatter–W and forward scatter–A parameters were used to exclude doublet cells, and 7-AAD solution (BD Biosciences) was used to discriminate between dead and living cells. Data were analyzed with FACSDiva (BD Biosciences) or FlowJo software (Tree Star).

Cell cycle, proliferation, and apoptosis analysis

For cell cycle analysis, BM cells were stained for cell-surface antigens, fixed, and permeabilized using FoxP3/Transcription Factor staining buffer set (Thermo Fisher Scientific) and labeled with Ki67-BV786 (B56) and 7-AAD (BD Bioscience). For proliferation experiments, mice were injected intraperitoneally with 1 mg EdU (Jena Bioscience), and BM cells were harvested 24 h later. Cells were stained for cell-surface antigens, and the subsequent fixation/permeabilization and azide-alkyne cycloaddition steps were performed using the Click-iT Plus EdU Flow Cytometry Assay Kit (Life Technologies). For evaluation of apoptosis, after staining for cell-surface antigens, cells were incubated at 37°C for 20 min in 500 μl preheated PBS plus 3% FBS supplemented with JC-1 dye (Mitochondrial Membrane Potential

Probe; ThermoFisher Scientific; final concentration 2.5 µg/ml). Cells were washed twice in preheated PBS plus 3% FBS and analyzed by flow cytometry.

Protein synthesis measurement

For L-homopropargylglycine incorporation assay, 4 × 10^6 BM cells or transduced TF-1 cells were incubated for 40 min at 37°C in 24-well plates in 1 ml RPMI 1640 without methionine (Gibco) supplemented with 10% FBS (Gibco). L-homopropargylglycine (Jena Bioscience; 50 µM final concentration) was added to the culture medium for 1 h 50 min, and then cells were collected and washed with 1% BSA in PBS. Cells were stained for cell-surface antigens as described earlier. The subsequent fixation/permeabilization and azide-alkyne cycloaddition steps were performed using the Click-iT Plus EdU Flow Cytometry Assay Kit (Life Technologies). Cells were resuspended in 3% FBS in PBS and analyzed by flow cytometry.

For in vivo protein synthesis measurement, mice were injected intraperitoneally with 1 mg O-propargyl-puromycin (Jena Bioscience), and BM cells were harvested 1 h later. The subsequent staining, fixation/permeabilization, and azide-alkyne cycloaddition steps were the same as described for L-homopropargylglycine.

Western blot and nanocapillary immunoassays

BM and FACS-sorted MyPs or TF-1 cells pellets were resuspended in lysis solution (1% NP-40; 0.5% sodium deoxycholate; 0.1% SDS; 25 mM Tris-HCl, pH 7.6; 150 mM NaCl; complete protease inhibitor cocktail [Roche] and PhosSTOP phosphatase inhibitors [Roche]), incubated on ice for 30 min, and treated by tip sonication (Bioruptor; Diagenode; five times at level 5 and duty cycle 50%). Proteins were extracted by centrifugation (16,100 *g*) for 30 min at 4°C and quantified using the BCA method (Micro BCA protein Assay kit; Thermo Fisher Scientific). For Western blotting, 30 µg of proteins from total BM cells were mixed with loading buffer, incubated at 98°C for 5 min, separated by SDS-PAGE on Mini-PROTEAN TGX Precast Gels 4–20% (Bio-Rad), and transferred to 0.45 µm polyvinylidene fluoride membranes (Amersham Hybond-P; GE Healthcare). Membranes were blocked for 1 h in a solution containing 5% nonfat milk or 5% BSA and then incubated with specific antibodies O/N at 4°C, followed by HRP-conjugated antibodies applied for 1 h at room temperature (conjugated anti-mouse, anti-rabbit, 1:2,000; Cell Signaling Technologies). Membranes were developed with the SuperSignal West Femto chemiluminescence kit (Thermo Fisher Scientific). Proteins from MyPs were separated using the WES system (Automated Western Blots with Simple Western; ProteinSimple) following the manufacturer's recommendations for a 25-well plate protocol using a 12–230-kD kit. Briefly, MyPs protein extracts at a concentration of 0.2 mg/ml were used, and eIF2α, phospho-Ser51eIF2α, and vinculin (Cell Signaling Technology) were used at 1/100, 1/10, and 1/1,000 dilution, respectively. Detection was performed with the Anti-Rabbit Detection Module for Jess, Wes, Peggy Sue, or Sally Sue (ProteinSimple). Proteins from TF-1 cells were separated using the Jess system (Automated Western Blots with Simple Western; ProteinSimple) with the normalization assay module (ProteinSimple) following the manufacturer's recommendations. TF-1 protein extracts at a concentration of 0.4 mg/ml were used, and TP53 antibody (Santa Cruz Biotechnology) was used at a 1/50 dilution and ELP3 (Cell Signaling Technology) and CTU2 (Novus) antibodies at a 1/10 dilution. Detection was performed with Anti-Mouse Detection Module for TP53 and Anti-Rabbit Detection Module for ELP3 and CTU2 (ProteinSimple). Data from Wes and Jess experiments were analyzed with Compass software (ProteinSimple).

Lentiviral infection of TF-1 cells

For silencing ELP3 and CTU2 expression, TF-1 cells were transduced with lentiviral particles. Lentiviral pLKO.1 human ELP3 shRNA vector (TRCN0000235508) and CTU2 shRNA vector (TRCN0000165286) were purchased from Sigma-Aldrich. Briefly, TF-1 cells were spin-infected in 6-well plates with concentrated lentivirus particles (multiplicity of infection = 10) and 5 µg/ml polybrene (Sigma-Aldrich). Cells were centrifugated at 800 *g* for 30 min and cultured overnight. These spin-infection steps were repeated the day after, and cells were selected 48 h after infection with 5 µg/ml puromycin. Knockdown efficiency was evaluated with nanocapillary immunoassay (Jess; ProteinSimple) analysis.

BM reconstitution experiments

12-wk-old recipient mice (CD45.1 or CD45.1-CD45.2) were lethally irradiated with two doses of 6 Gy 3 h apart using a Gammacell 40 Exactor (MDS Nordion). Cells were injected in the tail vein 2 h after the second irradiation. For HSC transplantation, 300 donor LT-HSCs were transplanted along with 0.3 × 10^6 competitor BM cells. Blood was collected from the tail vein of recipient mice, and chimerism was assessed every 4 wk for at least 16 wk after transplantation. Blood was incubated 10 min at room temperature in RBC lysis buffer (0.1 mM EDTA, 150 mM NH_4Cl, 10 mM $KHCO_3$) prior to staining. BM chimerism was evaluated 4 mo after transplantation.

For inducible BM transplantation, 10^6 donor BM cells from *Elp3*$^{fl/fl}$-*Mx1-Cre*$^{+/+}$ or *Elp3*$^{fl/fl}$-*Mx1-Cre*$^{T/+}$ were coinjected with 10^6 competitor total BM cells. Blood reconstitution was assessed after 4 wk. Mice then received four intraperitoneal injections of 250 µg poly(I:C) (InvivoGen) every other day 6 wk after transplantation to induce deletion of *Elp3* exon 2. Blood chimerism was measured every 4 wk for at least 16 wk after poly(I:C) injection, and BM chimerism was evaluated 16 wk after poly(I:C) injection. For secondary transplants, 2 × 10^6 BM cells collected from inducible primary recipients 4 mo after poly(I:C) injection were transplanted into irradiated CD45.1-CD45.2 recipient mice.

For homing assay, BM cells were harvested from *Elp3*$^{fl/fl}$ or *Elp3*^{HscKO} mice. 3 × 10^6 cells were phenotyped by flow cytometry to evaluate the BM composition, and 20 × 10^6 cells were injected into nonirradiated CD45.1 recipient mice. BM was collected 16 h after transplantation and cells were first enriched for lineage-negative cells by magnetism-activated cell sorting using a lineage cell depletion kit (Miltenyi Biotec) before staining for cell-surface antigens to evaluate HSC chimerism. HSC chimerism was corrected to the frequency of HSC in the donor BM.

5-FU treatment

To assess the reconstitution activity of LT-HSCs, mice were injected intraperitoneally with a single dose of 5-FU (Sigma-Aldrich; 150mg/kg) and peripheral blood counts were measured after 5 d. BM composition was analyzed after 9 d of treatment.

Transmission electron microscopy

For transmission electron microscopy analysis, 3 × 10^6 $CD127^-$ MyPs pooled from six $Elp3^{fl/fl}$ mice and 0.5 × 10^6 $CD127^-$ MyPs pooled from 10 $Elp3^{HscKO}$ mice were FACS sorted in PBS and mixed with B16 cells in a 1:2 ratio. Pellets were fixed for 2 h at 4°C in a solution composed of 2.5% glutaraldehyde in 0.1 M Sörensen's buffer (0.2 M NaH_2PO_4, 0.2 M Na_2HPO_4, pH 7.4). After several washes in the same buffer, the samples were postfixed for 60 min with 2% osmium tetroxide, washed in deionized water, dehydrated through graded ethanol (70%, 95%, and 100%), and embedded in epon for 48 h at 60°C.

Ultrathin sections (700-Å thick) were obtained by means of an ultramicrotome (Reichert Ultracut E) equipped with a diamond knife. The ultrathin sections were mounted on palladium/copper grids coated with collodion and contrasted with uranyl acetate and lead citrate for 5 min each before being examined under a Jeol JEM1400 transmission electron microscope at 80 kV.

Sample preparation for proteome analysis

For comparative proteomic analysis, 10^6 $CD127^-$ MyPs pooled from 12–14 $Elp3^{fl/fl}$ and 26–38 $Elp3^{HscKO}$ mice were FACS sorted in biological triplicate in PBS. Pellets were snap frozen and stored at −80°C before processing. Cell pellets were lysed in radioimmunoprecipitation assay buffer. The lysates were centrifuged at 14,000 rpm for 10 min. After centrifugation, the supernatants were collected, and proteins were precipitated using the methanol-chloroform precipitation method. The protein pellets were resuspended in 50 µl of 0.1 M tetraethylammonium tetrahydroborate/0.1% Rapigest (Waters) buffer, reduced with tris(2-carboxyethyl)phosphine for 60 min at 55°C, and then alkylated with iodoacetamide for 30 min at room temperature in the dark. The denatured proteins were digested with trypsin by incubating overnight at 37°C. The peptide concentration of the tryptic digest was determined by amino acid analysis using Hitachi L-8900 Amino Acid Analyzer.

6-Plex tandem mass tag (TMT) tandem mass spectrometry (MS/MS) analysis

The tryptic digests were labeled with TMT-6plex isobaric reagents (Thermo Fisher Scientific) according to the manufacturer's instructions. Equal concentrations (5 µg) of tryptic digest (based on amino acid analysis) from three control samples were labeled with TMT reagents 126, 128, and 130, and three knockout samples were labeled with TMT reagents 127, 129, and 131. The six TMT-labeled samples were combined and dried via SpeedVac. For fractionation, the dried TMT-labeled mixture was redissolved in 200 µl of 0.06% TFA and injected into a Hewlett Packard 1090 LC (liquid chromatography) system. The peptides were separated and eluted over a C18 column (Vydac; 1 mm ID × 250 mm length, 5-µm particle size; cat#218TP51) using a gradient that starts at 2% B (80% acetonitrile/0.052% TFA) and increases to 100% B in 2 h at a flow rate of 0.100 ml/min. 60 200-µL fractions were collected over the peptide elution time and then pooled to generate 10 pools. Five fractions in the beginning, which correspond to the column void volume, and five fractions at the end, where no peak was observed, were excluded before pooling. The fractions were pooled in the following order: for 50 viable fractions, pool 1 consists of fractions 6, 16, 26, 36, and 46; pool 2 consists of fractions 7, 17, 27, 37, and 47; and so on. Pools were dried down via SpeedVac, resuspended in buffer A (0.1% formic acid in water), and subjected to mass spectrometric analysis.

The pools were analyzed by LC-MS/MS on a Q-Exactive Plus mass spectrometer interfaced with a nanoACQUITY UPLC System at the front end. Samples were loaded into a trapping column (nanoACQUITY UPLC Symmetry C18 Trap Column, 180 µm × 20 mm, product # 186006527) at a flow rate of 5 µl/min and separated with a C18 column (nanoACQUITY column Peptide BEH C18, 75 µm × 250 mm, product # 186003545). The peptides were eluted with buffer B (0.1% formic acid in acetonitrile) gradient from 5% to 35% in 110 min at a flow rate of 300 nl/min.

LC-MS/MS data were acquired using the Top-20 data-dependent acquisition method. Full-scan MS spectra (m/z range, 200–2,000) were acquired with a resolution of 70,000, automatic gain control target of $1e^6$, and maximum injection time of 30 ms. MS/MS scans were acquired with a resolution of 17,500, automatic gain control target of $2e^5$, and maximum injection time of 50 ms. The precursor ions were selected with an isolation window of 1.5 m/z and fragmented by higher-collisional energy dissociation with normalized collision energies set to 27 and 32. Dynamic exclusion was set to 15 s to keep the repeat sequencing of peptides to minimum.

Protein identification and quantification

MS raw files were processed using Proteome Discoverer v2.0 (Thermo Fisher Scientific) software. The files were searched against mouse SwissProt database (downloaded in September 2015; number of protein entries = 16,710) using the Sequest HT algorithm. The search parameters include 10 ppm precursor mass tolerance and 0.6 daltons fragment mass tolerance. TMT-6plex (229.1629) on the N terminus and lysine and carbamidomethyl (57.02146) on cysteine were defined as static modifications. Oxidation on methionine (15.9949) was defined as dynamic modification. Peptide spectrum matches were verified based on q-values set to 1% false discovery rate using Percolator. Peptide relative protein quantification was also performed using Proteome Discoverer. For quantification, 50 ppm was used as an integration tolerance for reporter ion peaks.

Analysis of proteomic data

Differential protein expression between $Elp3^{fl/fl}$ and $Elp3^{HscKO}$ MyPs was analyzed using an adapted workflow (Kammers et al., 2015) of the limma package in R (Ritchie et al., 2015), which relies on an empirical Bayes moderated *t* test after fitting a linear model to the data. To reduce the impact of potential false-positive identification, we retained only high-confidence

peptides and proteins with two or more unique peptides quantified. Peptides were mapped to mouse proteins using the biomaRt package in R (Durinck et al., 2009). Proteins with moderate p- and q-values <0.05 (Fig. 3, A–C) or moderated q-value <0.1 (Fig. 4 C) were considered as significantly regulated. Network analysis was performed using the STRING application in Cytoscape v3.6 (Shannon et al., 2003). Disconnected nodes were masked and only edges with protein–protein interaction confidence coefficient >0.7 were selected. Gene Ontology Biological process enrichment analyses were performed using default statistical overrepresentation tests in PANTHER v13.1 or default overrepresentation enrichment analysis in Webgestalt using the lists of downregulated or upregulated proteins in *Elp3*^{HscKO} MyPs as input.

Codon bias analysis

The coding sequence (cds) of all protein-coding *Mus musculus* genes (genome assembly GRCm38.p6) was downloaded from Ensembl (http://www.ensembl.org). Codon frequency of AAA, CAA, and GAA in the complete cds of every Mouse Genome Informatics–annotated mouse gene was computed using the seqinr (Charif and Lobry, 2007) and biomaRt packages in R. We next computed a z-score for AAA, CAA, and GAA codon enrichment/depletion in the cds of the proteins found to be downregulated in *Elp3*^{HscKO} MyPs in our comparative proteomic analysis using the formula: z = (codon frequency of gene − average codon frequency in all mouse cds)/variance of codon frequency in all mouse cds. A heatmap was subsequently generated using the pheatmap package in R.

Total RNA isolation and RNA sequencing

For RNA sequencing of MyPs, 9 × 10^4 CD127$^-$ MyPs from two *Elp3*$^{fl/fl}$ and four to six *Elp3*^{HscKO} mice were FACS sorted in triplicate in 1 ml TRIzol Reagent (Thermo Fisher Scientific). RNA was extracted using Direct-zol RNA MiniPrep Plus (Zymo Research) and cleared of potential DNA contamination using the RNeasy MinElute Cleanup Kit (Qiagen). cDNA was synthesized with 10 ng of total RNA using the SMART-Seq v4 Ultra Low input RNA Kit for Sequencing (Clontech Laboratories) and amplified by seven cycles of locked-DNA PCR. For LT-HSC RNA sequencing, 1,500 *Elp3*$^{fl/fl}$ LT-HSCs or 9,000 *Elp3*^{HscKO} LT-HSCs from four *Elp3*$^{fl/fl}$ and four *Elp3*^{HscKO} mice in triplicate were directly FACS-sorted in 2 µl reaction buffer from SMART-Seq v4 Ultra Low input RNA Kit. cDNA was generated directly from the cells, and 14 cycles of locked-DNA PCR were used for cDNA amplification. One sample of *Elp3*^{HscKO} LT-HSCs yielded very low cDNA amplification and was discarded. The sequencing library for both LT-HSCs and MyPs was generated using the Nextera XT DNA Library Preparation (Illumina) according to manufacturer's instructions. Paired-end RNA sequencing was performed on a HiSeq 2000 (Illumina).

Analysis of RNA sequencing data

Sequenced reads were aligned to the mouse genome (University of California, Santa Cruz mm10) and aligned and mapped to mm10 with RNA-seq Alignment (v1.1.1) using TopHat 2 (Bowtie 2) on BaseSpace (https://basespace.illumina.com). Uniquely mapped reads were used to calculate gene expression. Differential gene expression was calculated using DESeq2 in R (Love et al., 2014). Genes with normalized P values <0.05 were considered as significantly regulated. GSEAR analyses on differentially expressed genes were performed on preranked list of such genes ordered according to their log2 fold change. Online GSEAR v6.0.10 (https://genepattern.broadinstitute.org/gp/pages/index.jsf) was used with either the "h.all.v6.1.symbols" (Hallmarks) or "C5.bp. v6.1.symbols" (gene ontology [GO] biological process) gene sets and default parameters, except for a "classic" scoring scheme and maximum gene set size of 250 and minimal gene set size of 20.

Polysome profiling

For polysome profiling analysis, 1–2 × 10^6 CD127$^-$ MyPs pooled from five *Elp3*$^{fl/fl}$ and 10 *Elp3*^{HscKO} mice were FACS sorted in biologic triplicate. Pellets were lyzed in hypotonic buffer as in Liang et al. (2018), and 10% of each sample, corresponding to total RNA, were directly lyzed in Trizol and snap frozen. The remaining cells were further loaded in a nonlinear gradient as described in Liang et al. (2018). Fractions corresponding to heavy polysomes were pooled, lyzed in Trizol, and snap frozen. RNA extraction, cDNA amplification, and library preparation and sequencing were performed as described in Total RNA isolation and RNA-sequencing in Materials and methods. Enrichment/depletion in heavy polysomal fraction was calculated in polysomal fractions vs. total RNA using DESeq2, and transcripts with adjusted P value <0.05 were considered as significantly enriched/depleted. The relative enrichment/depletion in Elp3-deficient MyPs compared with controls was calculated by dividing the fold change enrichment/depletion in heavy polysomal fraction in *Elp3*^{HscKO} MyPs by that in *Elp3*$^{fl/fl}$ MyPs. A difference of 30% was considered significant.

Real-time PCR analysis

Expression of *Ppp1r15a* and ER-associated degradation genes in MyPs was measured by real-time quantitative PCR analysis. RNA and cDNA were extracted and synthesized as described for RNA-sequencing. Quantitative real-time PCR was performed in duplicate with 100 pg cDNA using iTaq Universal SYBR Green supermix (Bio-Rad) and 7900HT Sequence Detection System (Applied Biosystems) under the following conditions: initial denaturation at 95°C for 15 min followed by 40 cycles of 95°C, 15 s and 60°C, 1 min. Primer sequences were as follows: 5′-CGAGGAGGAGGACAAGAAGG-3′ and 5′-GTTGGCTATGATCTCCACGC-3′ for *Grp78*; 5′-GCTACTGGAGTTCTATGCACC-3′ and 5′-GCTGAGGTTGCATCGATCTT-3′ for *Pdia4;* 5′-AGTTCGCCTTCCAAGCTGAA-3′ and 5′-TCAGTTAGGGAGATGAGCCT-3′ for *Grp94;* 5′-TCCAGGTCTTCGAAGCTACG-3′ and 5′-TGGGCCATGTACAACAATTCA-3′ for *EDEM-1;* 5′-GCCTCAGAGCGACAAATCAA-3′ and 5′-TGGCATCCGAGAGTGTTTCA-3′ for *Dnajb9*; and 5′-GACCCACGATCGCTTTTGG-3′ and 5′-GATAGAAGTTGTGGGCGTCC-3′ for *Ppp1r15a* genes. Expression levels of the genes of interest were normalized relative to control genes (5′-AGCCCAGTGTTACCACCAAG-3′ and 5′-ACCCAAGAACAAGCACAAGG-3′ for *Ubc*; 5′-GGCCTCTCAGAAGCATCACTA-3′ and 5′-GCCAAGCCCTGAGCATAA-3′ for *Tbp*; and 5′-CATGGCTCGCTCGGTGACC-3′ and

5′-AATGTGAGGCGGGTGGAACTG-3′ for *B2m*) using qBase+ software (Biogazelle).

XBP1 splicing

XBP1 splicing in MyPs was measured by semiquantitative PCR analysis. RNA was extracted and cDNA synthesized as described for RNA sequencing. Semiquantitative PCR was performed with 1 ng cDNA using GoTaq G2 Hot Start Taq Polymerase (Promega) under the following conditions: initial denaturation at 94°C for 90 s, followed by 38 cycles of 94°C, 30 s; 64°C, 45 s; and 72°C, 45 s. Primer sequences were as follows: 5′-TTACGGGAGAAAACT CACGGC-3′ and 5′-GGGTCCAACTTGTCCAGAATGC-3′. PCR products were separated on a 4% agarose gel, and band intensity was measured with ImageJ.

Targeted *Trp53* exon sequencing

DNA was extracted from paraformaldehyde-fixed thymus or spleen sections using a QIAamp DNA FFPE Tissue Kit (Qiagen). *Trp53* exons were amplified by high-fidelity PCR (Q5 High-Fidelity DNA Polymerase; New England BioLabs) using 14 flagged primer pairs: F1: 5′-TCGTCGGCAGCGTCAGATGTGTATAAG AGACAGTTTGTGCCAGGAGTCTCG-3′ and R1: 5′-GTCTCGTGG GCTCGGAGATGTGTATAAGAGACAGCGTCACGCTCATCAATT ACTTA-3′; F2: 5′-TCGTCGGCAGCGTCAGATGTGTATAAGAGA CAGAAGCCATAGGGGTTTGTTTG-3′ and R2: 5′-GTCTCGTGG GCTCGGAGATGTGTATAAGAGACAGCTTAAGGGCCCCAAAAA GAT-3′; F3: 5′-TCGTCGGCAGCGTCAGATGTGTATAAGAGACAG AACTCTCTGCTCTTGTTTTCCA-3′ and R3: 5′-GTCTCGTGGGCT CGGAGATGTGTATAAGAGACAGGTGACAGGGTCCTGTGCTG-3′; F4: 5′-TCGTCGGCAGCGTCAGATGTGTATAAGAGACAGTTTTGA AGGCCCAAGTGAAG-3′ and R4: 5′-GTCTCGTGGGCTCGGAGA TGTGTATAAGAGACAGCTGAAGAGGAACCCCCAAAT-3′; F5: 5′-TCGTCGGCAGCGTCAGATGTGTATAAGAGACAGCCGTTCTCT CTCCTCTCTTCC-3′ and R5: 5′-GTCTCGTGGGCTCGGAGATGT GTATAAGAGACAGGCGGTGTTGAGGGCTTAC-3′; F6: 5′-TCG TCGGCAGCGTCAGATGTGTATAAGAGACAGTCCCGGCTTCTG ACTTATTC-3′ and R6: 5′-GTCTCGTGGGCTCGGAGATGTGTA TAAGAGACAGGACGCACAAACCAAAACAAA-3′; F7: 5′-TCGTCG GCAGCGTCAGATGTGTATAAGAGACAGGTAGGGAGCGACTTC ACCTG-3′ and R7: 5′-GTCTCGTGGGCTCGGAGATGTGTATAA GAGACAGCAGAAGCTGGGGAAGAAACA-3′; F8: 5′-TCGTCGGCA GCGTCAGATGTGTATAAGAGACAGTGCTGGTCCTTTTCTTGT CC-3′ and R8: 5′-GTCTCGTGGGCTCGGAGATGTGTATAAGAG ACAGTGAAGCTCAACAGGCTCCTC-3′; F9: 5′-TCGTCGGCAGCG TCAGATGTGTATAAGAGACAGTTGAGCTTCACCCCAAAGTC-3′ and R9: 5′-GTCTCGTGGGCTCGGAGATGTGTATAAGAGACAGAT GCGAGAGACAGAGGCAAT-3′; F10: 5′-TCGTCGGCAGCGTCA GATGTGTATAAGAGACAGTGTCCAGTGCTTCCATCTCA-3′ and R10: 5′-GTCTCGTGGGCTCGGAGATGTGTATAAGAGACAGGG AGGGAGGTCTGGGTAGAG-3′; F11: 5′-TCGTCGGCAGCGTCAGAT GTGTATAAGAGACAGCCCTACCCATAGTAGAAGCCATC-3′ and R11: 5′-GTCTCGTGGGCTCGGAGATGTGTATAAGAGACAGTA TGGCGGGAAGTAGACTGG-3′; F12: 5′-TCGTCGGCAGCGTCAGAT GTGTATAAGAGACAGGCTACCTGAAGACCAAGAAGG-3′ and R12: 5′-GTCTCGTGGGCTCGGAGATGTGTATAAGAGACAGGG CTGAGCCCTAGCTACAAG-3′; F13: 5′-TCGTCGGCAGCGTCA GATGTGTATAAGAGACAGGTCCCTTCTGCTGCCTTTTT-3′ and R13: 5′-GTCTCGTGGGCTCGGAGATGTGTATAAGAGACAGACCCT ATGAGGGCCCAAGAT-3′; and F14: 5′-TCGTCGGCAGCGTCAGAT GTGTATAAGAGACAGCCTACCCCACACCCTGTAAG-3′ and R14: 5′-GTCTCGTGGGCTCGGAGATGTGTATAAGAGACAGGCTGATAT CAACCTCTCAAAACC-3′.

The resulting 14 amplicons were next reamplified and indexed by high-fidelity PCR and sequenced on a MiSeq 500 (Illumina). Reads were subsequently aligned to the sequence of mouse chromosome 11 (GRCm38 build, downloaded from ftp://ftp.ensembl.org/pub/release-92/fasta/mus_musculus/dna/) by using a custom manifest with the DNA-Amplicon app (v1.1.0) on BaseSpace (https://basespace.illumina.com). Default parameters were used, except for the search for somatic variants with a frequency >30%. Single-nucleotide variants and indels that passed the quality and frequency filters were subsequently mapped to the Trp53 mRNA and protein.

Quantification of tRNA modifications

Quantification of tRNA nucleoside modifications was performed by ArrayStar. Briefly, tRNA was isolated from total RNA samples (~5 µg, RNA integrity number > 9) by Urea-PAGE electrophoresis. A 60–90-nt band of tRNA was excised and purified by ethanol precipitation. Purified tRNA was quantified using Qubit RNA HS Assay kit (Q32855; Thermo Fisher Scientific). tRNA was hydrolysed to single nucleosides, and then nucleosides were dephosphorylated by an enzyme mix. Pretreated nucleoside solution was deproteinized using Satorius 10,000-D MWCO spin filter. LC-MS analysis of nucleoside mixtures was performed on an Agilent 6460 QQQ mass spectrometer with an Agilent 1260 HPLC system. Multireaction monitoring mode was performed because of its high selectivity and sensitivity attained working with parent-to-product ion transitions. LC-MS data were acquired using Agilent Qualitative Analysis software. Multireaction monitoring peaks of each of the 55 modified nucleosides were extracted and normalized to that of unmodified nucleosides. Differential presence of nucleoside modifications was calculated using DESeq2, and modified nucleosides with P values <0.1 were considered as significantly different.

Quantification and statistical analysis

All statistical analyses were performed using R (R Core Team, 2016). All experiments followed a randomized design. Sample sizes were determined by power analysis. Respect of tests assumptions and model fit were evaluated using diagnostic plots. Raw data were transformed when needed and back transformed for graphical presentation. Error bars in all graphs represent mean ± 95% confidence interval. Details on which analysis was performed in each experiment are provided in the figure legends. ANOVAs were followed by Tukey honestly significant difference (HSD) tests for multiple comparisons. A P value <0.05 was considered significant. For clarity of presentation, only results of intergroup comparisons of interest are displayed in figures.

Data availability

RNaseq data has been deposited on ArrayExpress (http://www.ebi.ac.uk/arrayexpress/experiments/E-MTAB-6992 and http://

www.ebi.ac.uk/arrayexpress/experiments/E-MTAB-9628). Proteomic data has been deposited on ProteomeXChange with accession code PXD010486. Other data sets generated during the current study are available from the corresponding author on reasonable request. Any data that support the findings of this study are available from the corresponding authors upon request.

Online supplemental material

Fig. S1 in relation with Fig. 1 shows additional characterization of *Elp3*^{HscKO} mice. Fig. S2 in relation with Fig. 2 provides information on cycling activity and survival of Elp3-deficient HSPCs, as well as additional transplantation assays. Fig. S3 in relation with Fig. 5 shows GSEAR analyses on differentially expressed genes in Elp3-deficient HSCs and MyPs, as well as intracellular flow cytometric assessment of p53 and Atf4 in Elp3-deficient HSPCs. Fig. S4 in relation with Fig. 8 provides PCA and GSEAR analyses on differentially expressed genes, as well as intracellular flow cytometric assessment of Atf4 and pSer51-eIF2α in *Elp3/Trp53*^{HscDKO} MyPs. Fig. S5 in relation with Fig. 9 shows location and representative pictures of tumors in *Trp53*^{HscKO}, *Elp3/Trp53*^{HscDKO}, and *Elp3*^{HscKO} mice. Table S1 provides the list of differentially expressed proteins in *Elp3*^{HscKO} compared with *Elp3*$^{fl/fl}$ MyPs. Table S2 contains the list of commonly differentially expressed genes in *Elp3*^{HscKO} HSCs and MyPs compared with control *Elp3*$^{fl/fl}$ counterparts. Table S3 lists commonly regulated genes in *Elp3*^{HscKO} vs. *Elp3*$^{fl/fl}$ and *Elp3/Trp53*^{HscDKO} vs. Trp53^{HscKO} MyPs.

Acknowledgments

The authors thank the Flow cytometry platform, the Mouse Facility, the GIGA-Genomics platform of GIGA Liege University, as well as the MS and Proteomics Resource at Yale University. They also thank R. Fares, C. François, and I. Sbai for excellent technical and secretarial assistance; C. Nieberding for counseling with statistical analyses; B. Charloteaux and D. Pirottin for help with bioinformatics analyses; and N. Jacobs for critical reading of the manuscript.

This work was funded by the Fonds de la Recherche Scientifique – FNRS (FRFS-WELBIO grant WELBIO-CR-2015S-01; C.J. Desmet), the FRIA fund of the Fonds de la Recherche Scientifique – FNRS (A. Rosu), the Léon Frédéricq Foundation of Liege University, and by Liege University. J. Jorssen is a Research Fellow, C.J. Desmet and F. Rapino are Research Associates, and A. Chariot and P. Close are Masters of Research of the Fonds de la Recherche Scientifique – FNRS.

Author contributions: Conceptualization, C.J. Desmet; methodology, A. Rosu and C.J. Desmet; investigation, A. Rosu, N. El Hachem, J. Jorssen, E. Ramery, F. Rapino, J. Somja, M. Thiry, M. Jacquemyn, and D. Daelemans; formal analysis, A. Rosu and C.J. Desmet; writing – original draft, A. Rosu and C.J. Desmet; writing – review and editing, K. Rouault-Pierre, F. Rapino, L. Nguyen, M. Thiry, D. Bonnet, A. Chariot, P. Close, and F. Bureau; funding acquisition, F. Bureau and C.J. Desmet; resources, K. Rouault-Pierre, C.M. Adams, L. Nguyen, M. Thiry, D. Bonnet, A. Chariot, and P. Close; supervision, C.J. Desmet.

Disclosures: The authors declare no competing interests exist.

Submitted: 8 April 2020
Revised: 23 October 2020
Accepted: 24 November 2020

References

Ben-Sahra, I., Hoxhaj, G., Ricoult, S.J.H., Asara, J.M., Manning, B.D. 2016. mTORC1 induces purine synthesis through control of the mitochondrial tetrahydrofolate cycle. *Science.* 351:728–733.

Charif, D., and J.R. Lobry. 2007. SeqinR 1.0-2: A Contributed Package to the R Project for Statistical Computing Devoted to Biological Sequences Retrieval and Analysis. *In* Structural Approaches to Sequence Evolution: Molecules, Networks, Populations. U. Bastolla, M. Porto, H.E. Roman, and M. Vendruscolo, editors. Springer, Heidelberg, Germany. 207–232. https://doi.org/10.1007/978-3-540-35306-5_10

Cheishvili, D., C. Maayan, R. Cohen-Kupiec, S. Lefler, M. Weil, G. Ast, and A. Razin. 2011. IKAP/Elp1 involvement in cytoskeleton regulation and implication for familial dysautonomia. *Hum. Mol. Genet.* 20:1585–1594. https://doi.org/10.1093/hmg/ddr036

Chou, H.-J., E. Donnard, H.T. Gustafsson, M. Garber, and O.J. Rando. 2017. Transcriptome-wide Analysis of Roles for tRNA Modifications in Translational Regulation. *Mol. Cell.* 68:978–992.e4. https://doi.org/10.1016/j.molcel.2017.11.002

Chua, B.A., I. Van Der Werf, C. Jamieson, and R.A.J. Signer. 2020. Post-Transcriptional Regulation of Homeostatic, Stressed, and Malignant Stem Cells. *Cell Stem Cell.* 26:138–159. https://doi.org/10.1016/j.stem.2020.01.005

Close, P., M. Gillard, A. Ladang, Z. Jiang, J. Papuga, N. Hawkes, L. Nguyen, J.P. Chapelle, F. Bouillenne, J. Svejstrup, et al. 2012. DERP6 (ELP5) and C3ORF75 (ELP6) regulate tumorigenicity and migration of melanoma cells as subunits of Elongator. *J. Biol. Chem.* 287:32535–32545. https://doi.org/10.1074/jbc.M112.402727

Delaunay, S., F. Rapino, L. Tharun, Z. Zhou, L. Heukamp, M. Termathe, K. Shostak, I. Klevernic, A. Florin, H. Desmecht, et al. 2016. Elp3 links tRNA modification to IRES-dependent translation of LEF1 to sustain metastasis in breast cancer. *J. Exp. Med.* 213:2503–2523. https://doi.org/10.1084/jem.20160397

Dey, S., T.D. Baird, D. Zhou, L.R. Palam, D.F. Spandau, and R.C. Wek. 2010. Both transcriptional regulation and translational control of ATF4 are central to the integrated stress response. *J. Biol. Chem.* 285:33165–33174. https://doi.org/10.1074/jbc.M110.167213

Durinck, S., P.T. Spellman, E. Birney, and W. Huber. 2009. Mapping identifiers for the integration of genomic datasets with the R/Bioconductor package biomaRt. *Nat. Protoc.* 4:1184–1191. https://doi.org/10.1038/nprot.2009.97

Ebert, S.M., M.C. Dyle, S.D. Kunkel, S.A. Bullard, K.S. Bongers, D.K. Fox, J.M. Dierdorff, E.D. Foster, and C.M. Adams. 2012. Stress-induced skeletal muscle Gadd45a expression reprograms myonuclei and causes muscle atrophy. *J. Biol. Chem.* 287:27290–27301. https://doi.org/10.1074/jbc.M112.374777

El Yacoubi, B., M. Bailly, and V. de Crécy-Lagard. 2012. Biosynthesis and function of posttranscriptional modifications of transfer RNAs. *Annu. Rev. Genet.* 46:69–95. https://doi.org/10.1146/annurev-genet-110711-155641

Gupta, R., and S. Laxman. 2020. tRNA wobble-uridine modifications as amino acid sensors and regulators of cellular metabolic state. *Curr. Genet.* 66:475–480. https://doi.org/10.1007/s00294-019-01045-y

Gupta, R., A.S. Walvekar, S. Liang, Z. Rashida, P. Shah, and S. Laxman. 2019. A tRNA modification balances carbon and nitrogen metabolism by regulating phosphate homeostasis. *eLife.* 8:e44795. https://doi.org/10.7554/eLife.44795

Guzzi, N., M. Ciesla, P.C.T. Ngoc, S. Lang, S. Arora, M. Dimitriou, K. Pimková, M.N.E. Sommarin, R. Munita, M. Lubas, et al. 2018. Pseudouridylation of tRNA-Derived Fragments Steers Translational Control in Stem Cells. *Cell.* 173:1204–1216.e26. https://doi.org/10.1016/j.cell.2018.03.008

Han, J., S.H. Back, J. Hur, Y.-H. Lin, R. Gildersleeve, J. Shan, C.L. Yuan, D. Krokowski, S. Wang, M. Hatzoglou, et al. 2013. ER-stress-induced transcriptional regulation increases protein synthesis leading to cell death. *Nat. Cell Biol.* 15:481–490. https://doi.org/10.1038/ncb2738

Hidalgo San Jose, L., M.J. Sunshine, C.H. Dillingham, B.A. Chua, M. Kruta, Y. Hong, D.M. Hatters, and R.A.J. Signer. 2020. Modest Declines in Proteome Quality Impair Hematopoietic Stem Cell Self-Renewal. *Cell Rep.* 30:69–80.e6. https://doi.org/10.1016/j.celrep.2019.12.003

Johansson, M.J., A. Esberg, B. Huang, G.R. Björk, and A.S. Byström. 2008. Eukaryotic wobble uridine modifications promote a functionally redundant decoding system. *Mol. Cell. Biol.* 28:3301–3312. https://doi.org/10.1128/MCB.01542-07

Kammers, K., R.N. Cole, C. Tiengwe, and I. Ruczinski. 2015. Detecting Significant Changes in Protein Abundance. *EuPA Open Proteom.* 7:11–19. https://doi.org/10.1016/j.euprot.2015.02.002

Karlsborn, T., H. Tükenmez, A.K.M.F. Mahmud, F. Xu, H. Xu, and A.S. Byström. 2014. Elongator, a conserved complex required for wobble uridine modifications in eukaryotes. *RNA Biol.* 11:1519–1528. https://doi.org/10.4161/15476286.2014.992276

Khajuria, R.K., M. Munschauer, J.C. Ulirsch, C. Fiorini, L.S. Ludwig, S.K. McFarland, N.J. Abdulhay, H. Specht, H. Keshishian, D.R. Mani, et al. 2018. Ribosome Levels Selectively Regulate Translation and Lineage Commitment in Human Hematopoiesis. *Cell.* 173:90–103.e19. https://doi.org/10.1016/j.cell.2018.02.036

Kotler, E., O. Shani, G. Goldfeld, M. Lotan-Pompan, O. Tarcic, A. Gershoni, T.A. Hopf, D.S. Marks, M. Oren, and E. Segal. 2018. A Systematic p53 Mutation Library Links Differential Functional Impact to Cancer Mutation Pattern and Evolutionary Conservation. *Mol. Cell.* 71:178–190.e8. https://doi.org/10.1016/j.molcel.2018.06.012

Kruiswijk, F., C.F. Labuschagne, and K.H. Vousden. 2015. p53 in survival, death and metabolic health: a lifeguard with a licence to kill. *Nat. Rev. Mol. Cell Biol.* 16:393–405. https://doi.org/10.1038/nrm4007

Krutyhołowa, R., K. Zakrzewski, and S. Glatt. 2019. Charging the code - tRNA modification complexes. *Curr. Opin. Struct. Biol.* 55:138–146. https://doi.org/10.1016/j.sbi.2019.03.014

Ladang, A., F. Rapino, L.C. Heukamp, L. Tharun, K. Shostak, D. Hermand, S. Delaunay, I. Klevernic, Z. Jiang, N. Jacques, et al. 2015. Elp3 drives Wnt-dependent tumor initiation and regeneration in the intestine. *J. Exp. Med.* 212:2057–2075. https://doi.org/10.1084/jem.20142288

Laguesse, S., C. Creppe, D.D. Nedialkova, P.-P. Prévot, L. Borgs, S. Huysseune, B. Franco, G. Duysens, N. Krusy, G. Lee, et al. 2015. A Dynamic Unfolded Protein Response Contributes to the Control of Cortical Neurogenesis. *Dev. Cell.* 35:553–567. https://doi.org/10.1016/j.devcel.2015.11.005

Laxman, S., B.M. Sutter, X. Wu, S. Kumar, X. Guo, D.C. Trudgian, H. Mirzaei, and B.P. Tu. 2013. Sulfur amino acids regulate translational capacity and metabolic homeostasis through modulation of tRNA thiolation. *Cell.* 154:416–429. https://doi.org/10.1016/j.cell.2013.06.043

Liang, S., H.M. Bellato, J. Lorent, F.C.S. Lupinacci, C. Oertlin, V. van Hoef, V.P. Andrade, M. Roffé, L. Masvidal, G.N.M. Hajj, and O. Larsson. 2018. Polysome-profiling in small tissue samples. *Nucleic Acids Res.* 46:e3. https://doi.org/10.1093/nar/gkx940

Liu, Y., C. Chen, Z. Xu, C. Scuoppo, C.D. Rillahan, J. Gao, B. Spitzer, B. Bosbach, E.R. Kastenhuber, T. Baslan, et al. 2016. Deletions linked to TP53 loss drive cancer through p53-independent mechanisms. *Nature.* 531:471–475. https://doi.org/10.1038/nature17157

Liu, X., Y. Zhang, M. Ni, H. Cao, R.A.J. Signer, D. Li, M. Li, Z. Gu, Z. Hu, K.E. Dickerson, et al. 2017. Regulation of mitochondrial biogenesis in erythropoiesis by mTORC1-mediated protein translation. *Nat. Cell Biol.* 19:626–638. https://doi.org/10.1038/ncb3527

Love, M.I., W. Huber, and S. Anders. 2014. Moderated estimation of fold change and dispersion for RNA-seq data with DESeq2. *Genome Biol.* 15:550. https://doi.org/10.1186/s13059-014-0550-8

Masuoka, H.C., Townes, T.M. 2002. Targeted disruption of the activating transcription factor 4 gene results in severe fetal anemia in mice. *Blood.* 99:736–745.

Park, Y., A. Reyna-Neyra, L. Philippe, and C.C. Thoreen. 2017. mTORC1 Balances Cellular Amino Acid Supply with Demand for Protein Synthesis through Post-transcriptional Control of ATF4. *Cell Rep.* 19:1083–1090. https://doi.org/10.1016/j.celrep.2017.04.042

Qing, G., B. Li, A. Vu, N. Skuli, Z.E. Walton, X. Liu, P.A. Mayes, D.R. Wise, C.B. Thompson, J.M. Maris, et al. 2012. ATF4 regulates MYC-mediated neuroblastoma cell death upon glutamine deprivation. *Cancer Cell.* 22:631–644. https://doi.org/10.1016/j.ccr.2012.09.021

R Core Team. 2016. R: A Language and Environment for Statistical Computing. https://www.r-project.org/ (accessed October 1, 2017).

Rapino, F., S. Delaunay, F. Rambow, Z. Zhou, L. Tharun, P. De Tullio, O. Sin, K. Shostak, S. Schmitz, J. Piepers, et al. 2018. Codon-specific translation reprogramming promotes resistance to targeted therapy. *Nature.* 558:605–609. https://doi.org/10.1038/s41586-018-0243-7

Ritchie, M.E., B. Phipson, D. Wu, Y. Hu, C.W. Law, W. Shi, and G.K. Smyth. 2015. limma powers differential expression analyses for RNA-sequencing and microarray studies. *Nucleic Acids Res.* 43:e47. https://doi.org/10.1093/nar/gkv007

Rouault-Pierre, K., L. Lopez-Onieva, K. Foster, F. Anjos-Afonso, I. Lamrissi-Garcia, M. Serrano-Sanchez, R. Mitter, Z. Ivanovic, H. de Verneuil, J. Gribben, et al. 2013. HIF-2α protects human hematopoietic stem/progenitors and acute myeloid leukemic cells from apoptosis induced by endoplasmic reticulum stress. *Cell Stem Cell.* 13:549–563. https://doi.org/10.1016/j.stem.2013.08.011

Shannon, P., A. Markiel, O. Ozier, N.S. Baliga, J.T. Wang, D. Ramage, N. Amin, B. Schwikowski, and T. Ideker. 2003. Cytoscape: a software environment for integrated models of biomolecular interaction networks. *Genome Res.* 13:2498–2504. https://doi.org/10.1101/gr.1239303

Signer, R.A., J.A. Magee, A. Salic, and S.J. Morrison. 2014. Haematopoietic stem cells require a highly regulated protein synthesis rate. *Nature.* 509:49–54. https://doi.org/10.1038/nature13035

Signer, R.A.J., L. Qi, Z. Zhao, D. Thompson, A.A. Sigova, Z.P. Fan, G.N. DeMartino, R.A. Young, N. Sonenberg, and S.J. Morrison. 2016. The rate of protein synthesis in hematopoietic stem cells is limited partly by 4E-BPs. *Genes Dev.* 30:1698–1703. https://doi.org/10.1101/gad.282756.116

Tameire, F., I.I. Verginadis, N.M. Leli, C. Polte, C.S. Conn, R. Ojha, C. Salas Salinas, F. Chinga, A.M. Monroy, W. Fu, et al. 2019. ATF4 couples MYC-dependent translational activity to bioenergetic demands during tumour progression. *Nat. Cell Biol.* 21:889–899. https://doi.org/10.1038/s41556-019-0347-9

Tang, X., M.M. Keenan, J. Wu, C.-A. Lin, L. Dubois, J.W. Thompson, S.J. Freedland, S.K. Murphy, and J.-T. Chi. 2015. Comprehensive profiling of amino acid response uncovers unique methionine-deprived response dependent on intact creatine biosynthesis. *PLoS Genet.* 11:e1005158. https://doi.org/10.1371/journal.pgen.1005158

Terao, C., A. Suzuki, Y. Momozawa, M. Akiyama, K. Ishigaki, K. Yamamoto, K. Matsuda, Y. Murakami, S.A. McCarroll, M. Kubo, et al. 2020. Chromosomal alterations among age-related haematopoietic clones in Japan. *Nature.* 584:130–135. https://doi.org/10.1038/s41586-020-2426-2

van Galen, P., A. Kreso, N. Mbong, D.G. Kent, T. Fitzmaurice, J.E. Chambers, S. Xie, E. Laurenti, K. Hermans, K. Eppert, et al. 2014. The unfolded protein response governs integrity of the haematopoietic stem-cell pool during stress. *Nature.* 510:268–272. https://doi.org/10.1038/nature13228

Waszak, S.M., G.W. Robinson, B.L. Gudenas, K.S. Smith, A. Forget, M. Kojic, J. Garcia-Lopez, J. Hadley, K.V. Hamilton, E. Indersie, et al. 2020. Germline Elongator mutations in Sonic Hedgehog medulloblastoma. *Nature.* 580:396–401. https://doi.org/10.1038/s41586-020-2164-5

Wortel, I.M.N., L.T. van der Meer, M.S. Kilberg, and F.N. van Leeuwen. 2017. Surviving Stress: Modulation of ATF4-Mediated Stress Responses in Normal and Malignant Cells. *Trends Endocrinol. Metab.* 28:794–806. https://doi.org/10.1016/j.tem.2017.07.003

Zinshteyn, B., and W.V. Gilbert. 2013. Loss of a conserved tRNA anticodon modification perturbs cellular signaling. *PLoS Genet.* 9:e1003675. https://doi.org/10.1371/journal.pgen.1003675

JEM

Supplemental material

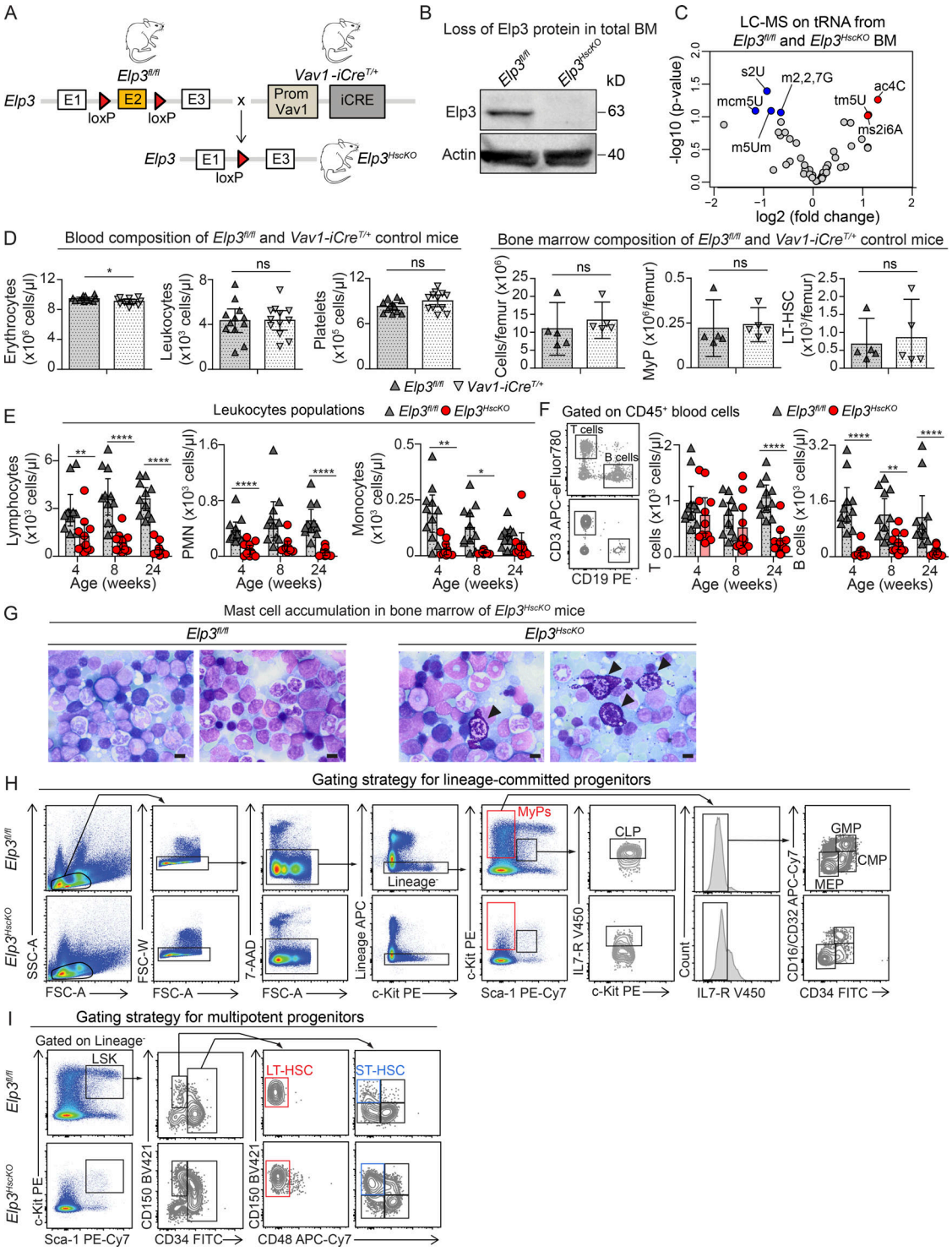

Figure S1. **Loss of Elongator activity in hematopoietic progenitors causes hematopoietic failure. (A)** Description of the crossing of *Elp3*$^{fl/fl}$ and *Vav-iCre*$^{T/+}$ mouse strains for the generation of *Elp3*^{HscKO} mice. **(B)** Western blot analysis of Elp3 protein expression in total BM cells from *Elp3*$^{fl/fl}$ and *Elp3*^{HscKO} mice (representative of three experiments). **(C)** LC-MS comparison of uridine base modifications in total BM cells from *Elp3*$^{fl/fl}$ and *Elp3*^{HscKO} mice. **(D)** Comparison of blood concentrations (left) of RBCs, leukocytes, and platelets and BM cellularity, MyP and LT-HSC numbers (right) in *Elp3*$^{fl/fl}$ and *Vav-iCre*$^{T/+}$ mice (two-way ANOVA followed by Tukey HSD tests, n = 5 or 12/group, data pooled from two or three experiments). **(E)** Hemocytometric comparison of blood concentrations in lymphocytes, polymorphonuclear, and monocytes in *Elp3*$^{fl/fl}$ and *Elp3*^{HscKO} mice (two-way ANOVA followed by Tukey HSD tests, n = 11/group, data pooled from three experiments). **(F)** Flow cytometric profile (left) and blood concentrations of T cells and B cells in *Elp3*$^{fl/fl}$ and *Elp3*^{HscKO} mice (two-way ANOVA followed by Tukey HSD tests, n = 11/group, data pooled from three experiments). **(G)** Representative May Grünwald–Giemsa staining of BM smear of 24-wk-old *Elp3*$^{fl/fl}$ and *Elp3*^{HscKO} mice (arrowheads, mast cell; scale bars, 10 µm). **(H and I)** Gating strategy for the flow cytometric identification of lineage-committed progenitor (H) and LSK multipotent progenitor (I) BM populations in Fig. 1, H and I. ns, not significant; *, P < 0.05, **; P < 0.01; ****, P < 1.10^{-4}. PMN, polymorphonuclear.

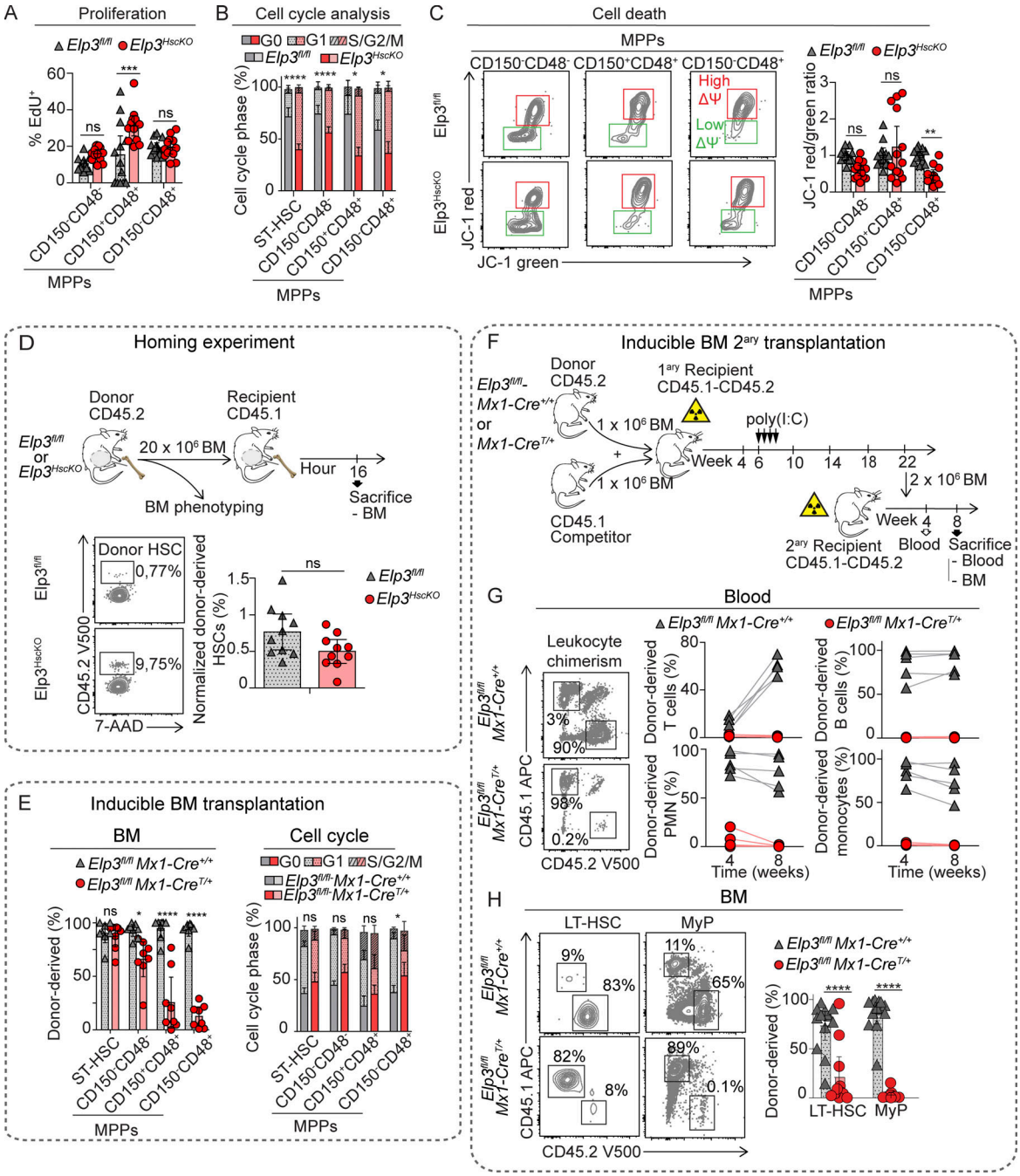

Figure S2. **Loss of Elongator activity kills progenitors and impairs HSC grafting activity. (A)** Flow cytometric profile (left) and percentages of proliferating cells (right) based on EdU incorporation (two-sided pairwise *t* tests followed by Bonferonni correction, *n* = 13–14/group, pool of three experiments). **(B)** Flow cytometric profile (left) and percentages of cells in the G0, G1, and S/G2/M phases of the cell cycle (right) based on Ki67 and 7-AAD signal intensity (two-sided pairwise *t* tests comparison of percent G0 followed by Bonferonni correction, *n* = 9/group, pool of three experiments). **(C)** Flow cytometric profile (left) and ratio of red-on-green signal intensities (normalized to the mean ratio in control cells in each experiment; Δψ, mitochondrial membrane potential; two-sided pairwise *t* tests followed by Bonferonni correction, *n* = 13/group, pool of three experiments) in HSPCs of *Elp3*$^{fl/fl}$ and *Elp3*^{HscKO} mice. **(D)** Experimental outline of homing assays of *Elp3*$^{fl/fl}$ and *Elp3*^{HscKO} total BM cells and flow cytometric profile of HSC chimerism. Chimerism of HSC in recipient mice was corrected to the percentage of HSC in donor BM cells (two-sided *t* test, *n* = 10/group, data representative of two independent experiments). **(E)** HSPC chimerism (left) and percentages of cells in the G0, G1, and S/G2/M phases of the cell cycle based on Ki67 and 7-AAD signal intensity (right) in transplant-recipient mice in competitive transplantation assays of *Elp3*$^{fl/fl}$ or *Elp3*$^{fl/fl}$ *Mx1-Cre*$^{T/+}$ BM along equal numbers of competitor WT BM cells, followed by induction of floxed allele recombination by poly(I:C) treatment (two-sided pairwise *t* tests followed by Bonferonni correction, comparison of percent G0 in E, *n* = 8–9/group, data representative of two experiments; ns, not significant; *, P < 0.05; ****, P < 1.10^{-4}). **(F)** Experimental outline of competitive secondary transplantation assays of *Elp3*$^{fl/fl}$ or *Elp3*$^{fl/fl}$ *Mx1-Cre*$^{T/+}$ total BM cells along equal numbers of competitor WT BM cells. **(G and H)** Flow cytometric profile (left) and resulting *Elp3*$^{fl/fl}$ or *Elp3*$^{fl/fl}$ *Mx1-Cre*$^{T/+}$ blood leukocyte (G) or BM LT-HSC and MyP (H) chimerism through time (right) in transplant-recipient mice (two-way ANOVA followed by Tukey HSD tests, *n* = 5–6/group, data representative of two independent experiments). ns, not significant; *, P < 0.05; **, P < 0.01; ***, P < 0.001; ****, P < 1.10^{-4}.

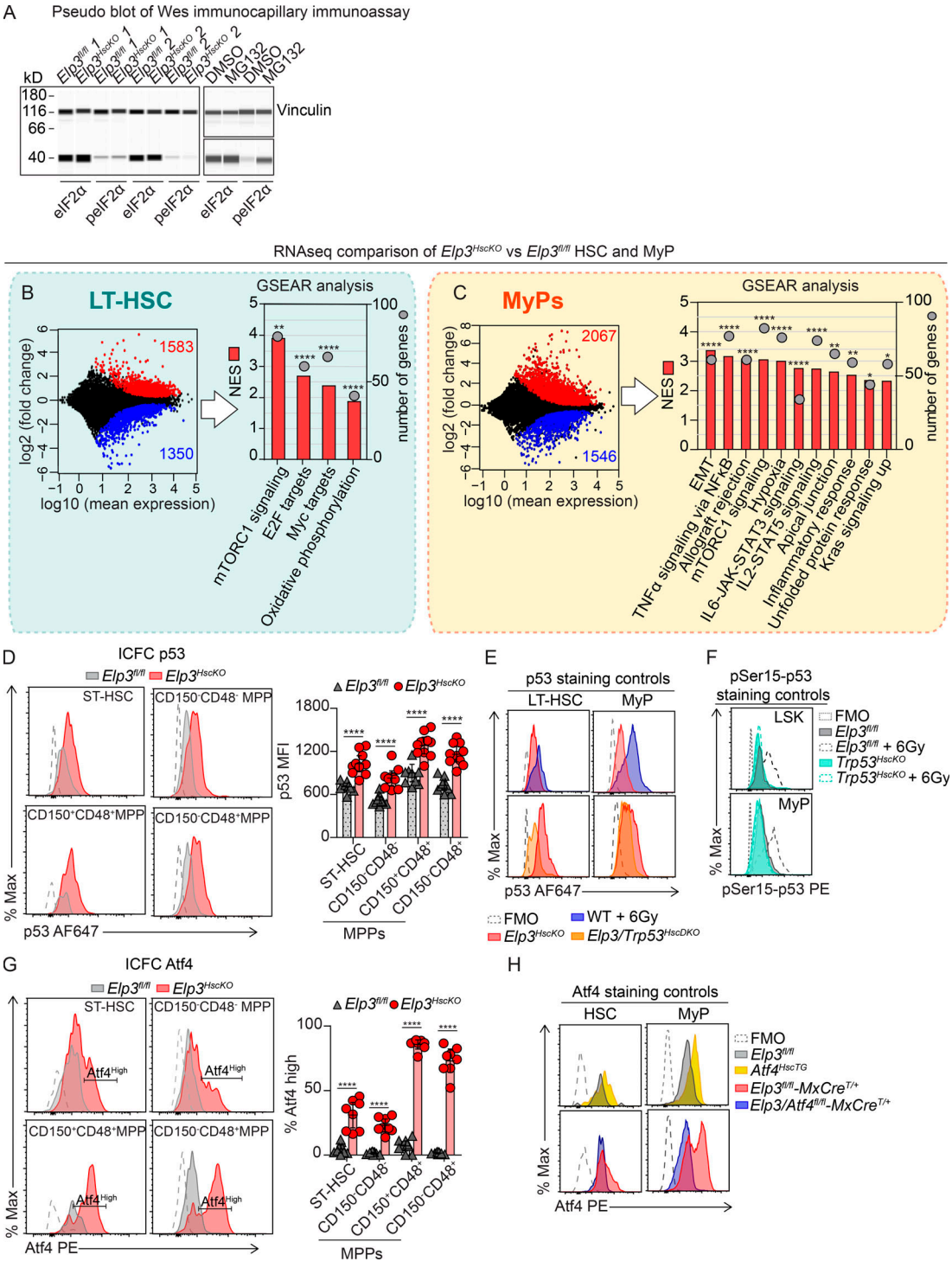

Figure S3. **Deficiency in Elongator activates the p53 and Atf4 stress response pathways in hematopoietic progenitors. (A)** Representative pseudoblot of eIF2α and phospho-Ser51eIF2α (lower bands) protein expression on protein extracts of *Elp3*$^{fl/fl}$ and *Elp3*^{HscKO} MyPs obtained by Wes nanocapillary immunoassay. Vinculin was used as loading control for quantification (upper band, positive control MG132-treated BM). **(B and C)** MA plots of the changes in mRNA expression in *Elp3*^{HscKO} vs. *Elp3*$^{fl/fl}$ LT-HSCs (B) and MyPs (C; left, same data as in Fig. 3 A for MyPs) and GSEAR analysis of upregulated Hallmark MSigDb gene sets (right, *, FWER P < 0.05; **, FWER P < 0.01; ****, FWER P < 1.10^{-4}). **(D)** Intracellular flow cytometric profile of nuclear p53 expression (left) and comparison of the p53 signal intensity (right) in *Elp3*$^{fl/fl}$ and *Elp3*^{HscKO} HSPCs (two-way ANOVA followed by Tukey HSD tests, *n* = 10/group, data pooled from three experiments). **(E)** Flow cytometric profile of p53 signal in LT-HSCs and MyPs from *Elp3*^{HscKO} 6-Gy irradiated or *Elp3/Trp53*^{HscDKO} mice as positive and negative staining control, respectively. **(F)** Flow cytometric profile of phospho-Ser15-p53 expression in LSK and MyP from *Elp3*$^{fl/fl}$ or *Trp53*^{HscKO} mice 6-Gy irradiated or not as positive and negative staining control, respectively. **(G)** Intracellular flow cytometric (ICFC) profile of Atf4 expression (left) and comparison of the percentages of Atf4^{high} cells (right) in *Elp3*$^{fl/fl}$ and *Elp3*^{HscKO} HSPCs (****, P < 1.10^{-4} in a two-way ANOVA followed by Tukey HSD tests, *n* = 8–9/group, data pooled from two experiments). **(H)** Flow cytometric profile of Atf4 expression in HSCs and MyPs from *Elp3*$^{fl/fl}$, *Elp3*$^{fl/fl}$ *MxCre*$^{T/+}$, *Atf4*^{HscTG}, or *Elp3/Atf4*$^{fl/fl}$ *MxCre*$^{T/+}$ mice as positive and negative staining control, respectively. FMO, fluorescence minus one; NES, normalized enrichment score. ****, P < 1.10^{-4}.

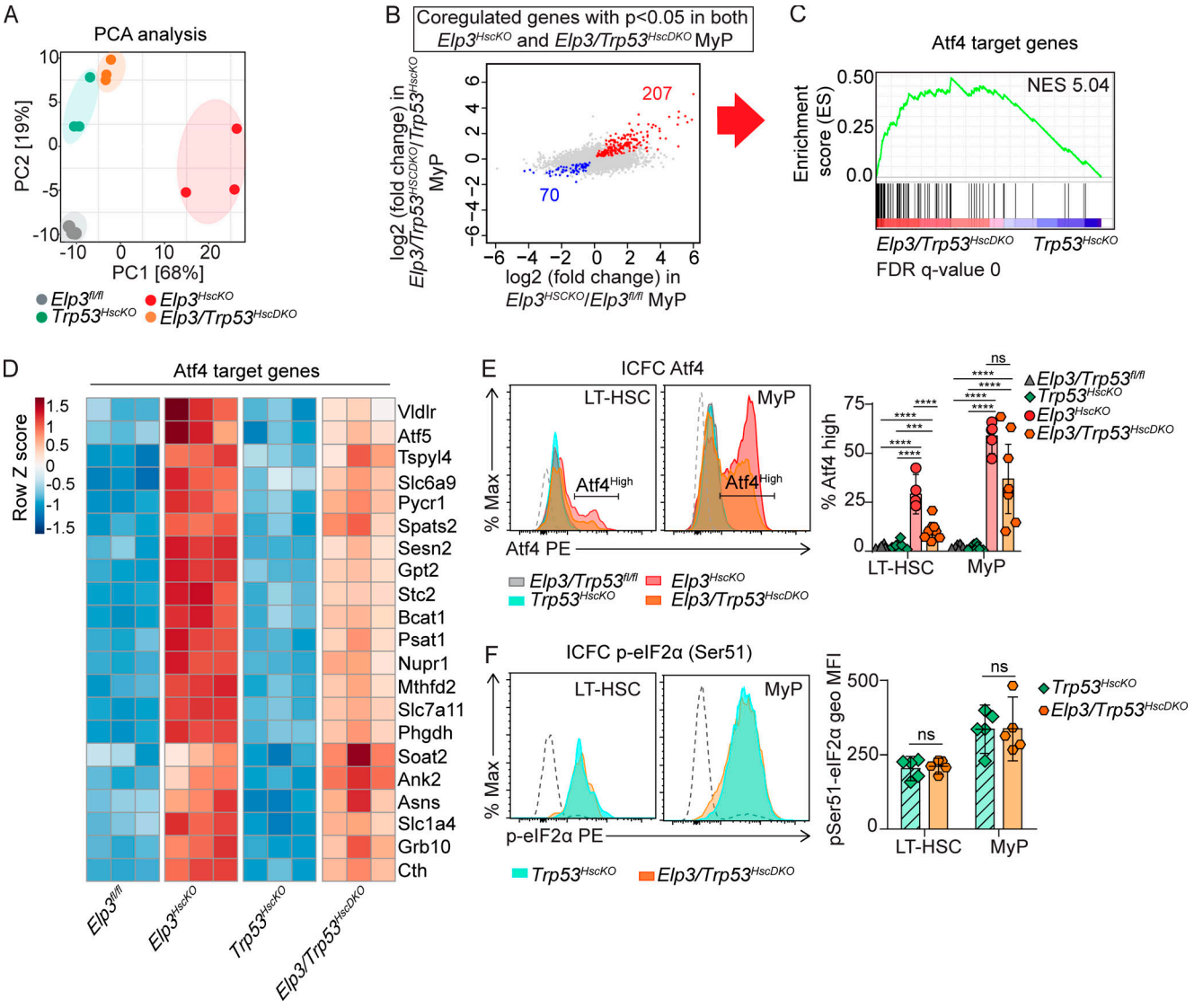

Figure S4. **Deletion of p53 rescues Elongator-deficient hematopoiesis. (A)** Principal component analysis on the transcriptome of *Elp3*$^{fl/fl}$, *Trp53*^{HscKO}, *Elp3*^{HscKO}, and *Elp3/Trp53*^{HscDKO} MyPs. **(B)** Correlation between changes in mRNA expression in *Elp3*^{HscKO} vs. *Elp3*$^{fl/fl}$ MyPs and in *Elp3/Trp53*^{HscDKO} vs. *Trp53*^{HscKO} MyPs. **(C)** GSEAR analysis of Atf4 target genes in genes coregulated in both *Elp3*^{HscKO} and *Elp3/Trp53*^{HscDKO} MyPs compared with their *Elp3*$^{fl/fl}$ or *Trp53*^{HscKO} counterparts. **(D)** Heatmap of the expression of the top 20 leading edge Atf4 target genes in *Elp3*$^{fl/fl}$, *Trp53*^{HscKO}, *Elp3*^{HscKO}, and *Elp3/Trp53*^{HscDKO} MyPs. **(E and F)** Intracellular flow cytometric (ICFC) profile of Atf4 (E) and phospho-Ser51 eIF2α signal (F) in *Elp3*$^{fl/fl}$, *Trp53*^{HscKO}, *Elp3*^{HscKO}, and *Elp3/Trp53*^{HscDKO} HSCs and MyPs (ns, not significant; ***, P < 0.001; ****, P < 1.10^{-4} in a two-way ANOVA followed by Tukey HSD tests, *n* = 5–8/group, data pooled from two experiments). FDR, false discovery rate; NES, normalized enrichment score.

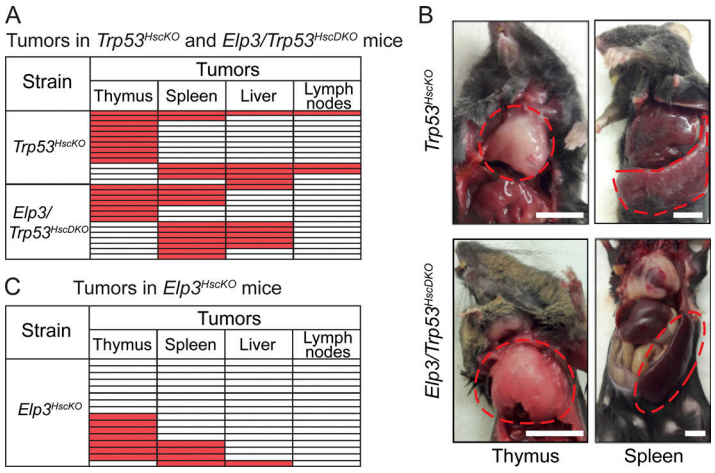

Figure S5. **p53 is activated as an antitumor checkpoint in Elongator-deficient hematopoietic progenitors. (A and B)** Tumor-bearing organs in *Trp53*^{HscKO} and *Elp3/Trp53*^{HscDKO} mice reaching ethical end points (A) and representative pictures of such tumors (B; scale bars, 1 cm). **(C)** Incidence of tumors and tumor-bearing organs in *Elp3*^{HscKO} mice reaching ethical end points.

Provided online are three tables. Table S1 lists differentially expressed proteins in *Elp3*^{HscKO} compared with *Elp3*$^{fl/fl}$ MyPs. Table S2 lists commonly differentially expressed genes in *Elp3*^{HscKO} HSCs and MyPs compared with control *Elp3*$^{fl/fl}$ counterparts. Table S3 lists commonly regulated genes in *Elp3*^{HscKO} vs. *Elp3*$^{fl/fl}$ and *Elp3/Trp53*^{HscDKO} vs. *Trp53*^{HscKO} MyPs.